

**Application of X-Ray Parametric Down-
Conversion for Nonlinear X-Ray
Spectroscopy and Quantum Optics**

Denis Borodin

Department of Physics

Ph.D. Thesis

Submitted to the Senate of Bar-Ilan University

Ramat-Gan, Israel

December, 2018

This work was carried under the supervision of

Prof. Sharon Shwartz

Department of Physics

Bar-Ilan University

Acknowledgments

I would like to thank my supervisor Prof. Sharon Shwartz for introducing me to the exciting field of nonlinear x-ray optics and for his help and guidance throughout my PhD programme.

I would like to express my gratitude to Mrs. Hila Schwartz for her assistance and support with all sorts of issues that showed up during my research.

I would like to express my sincere appreciation to the administrative staff of the physics department, Rachel Rothberg, Rita Golender, and Yossi Ben-Zion for their help and assist with my issues that I had met during my PhD.

I want to thank Dr. Aviad Schori for his participation in the synchrotron experiments and help with the development of analysis and data acquisition programs. I also thank Mr. Edward Strizevsky for participating in synchrotron experiments.

Finally, I would like to thank my family for supporting me and believing in me all these years.

Table of contents

Abstract.....	i
1. Introduction and background.....	1
1.1. Literature review.....	1
1.1.1. X-ray into x-ray PDC.....	3
1.1.2. Nonlinear x-ray spectroscopy.....	5
1.2. The coupled wave equations.....	10
1.3. Nonlinear current density.....	12
2. X-ray PDC as a source of paired photons.....	15
2.1. X-ray photon pairs with highly suppressed background.....	15
2.1.1. Introduction.....	15
2.1.2. Theoretical basis.....	16
2.1.3. The experiment.....	19
2.1.4. Results and discussion.....	21
2.2. Joint works.....	25
3. Nonlinear x-ray spectroscopy.....	29
3.1. Evidence for collective interactions in x-ray into UV PDC.....	29
3.1.1. Introduction.....	29
3.1.2. The model.....	30
3.1.3. The experiment and procedure.....	33
3.1.4. Spectral measurements and discussion.....	35
3.2. Nonlinear optical response in metals.....	37
3.2.1. Introduction.....	37
3.2.2. Substantiation of the experiment.....	38
3.2.3. Aluminum spectra and discussion.....	40

3.3. High-energy resolution measurements of x-ray into UV PDC with an x-ray tube source.....	42
3.3.1. Introduction.....	42
3.3.2. Experimental setup and noise level evaluation.....	44
3.3.3. Experimental procedure and results.....	47
3.3.4. Spectrum of LiF and discussion.....	51
4. Conclusions and outlook.....	53
4.1. Summary of my works.....	53
4.2. Further studies.....	55
Bibliography.....	57
Appendix A - Solution of the coupled wave equations in the Heisenberg-Langevin picture.....	63
Appendix B - Derivation of the nonlinear current density.....	66
Appendix C - Papers published in peer review journals.....	73
Abstract Hebrew.....	κ

List of Figures

- 1.1 - x-ray PDC phase-matching scheme. The indices p , s , and i represent the pump, the signal, and the idler, respectively, G is the reciprocal lattice vector.....2
- 1.2 SFG signal energy versus analyzer angle. Inset shows energy relative to the x-ray pump at 8 keV. Black line represents the Gaussian fit. The image is taken from Ref. 27.....6
- 1.3 Three-dimensional view of normalized linear susceptibility at 60 eV idler energy. Carbon atoms are in the blue spheres, solid lines represent the binding electrons. The image is taken from Ref. 36.....9
- 2.1 (a) Phase-matching scheme. (b) Schematic of the experimental setup. The indices p, s , and i are for the pump, signal, and idler respectively, \vec{G} represents the reciprocal lattice vector orthogonal to the (660) atomic planes and \hat{e} is a polarization vector. D1 and D2 indicate the two detectors.....17
- 2.2 Coincidence electronic circuit. The detectors $D1$ and $D2$ produce logic signals that trigger the logical unit AND. When the coincidence event occurs, the analog signals from detector's multi-channel analyzers are recorded by the digitizer.....19
- 2.3 Typical raw spectrum measured by a single detector. The Compton peak is at the calculated photon energy. The peak with the energy shift of 1.5 keV from the elastic is the escape peak. The inset shows the structure at the energies of interest. Several fluorescence peaks originated mainly from elements such as iron and lead are clearly seen in the range of 6 keV – 15 keV.....20
- 2.4 Energy histograms of the measured coincidence count rate at the degeneracy for detectors $D1$ and $D2$ are depicted on a) and b) respectively. Raw coincidence data and results of applying the energy conservation filter, i.e. the

sum of the energies of each coincidence event equals to the pump energy within an energy window of 500 eV. Solid lines are theoretical calculations.....	22
2.5 Coincidence diagrams after applying the energy conservation filter for the cases off the degeneracy a) $\omega_s / \omega_{s0} = 1.2$ and b) $\omega_s / \omega_{s0} = 1.4$	23
2.6 Calculation of the second-order correlation function for several phase-matching configurations for the case of degenerate energy. Δ is the offset from the Bragg angle. The correlation time is the smallest when the offset is the smallest, i.e. the generated photons are nearly collinear.....	24
2.7 Coincidence spectra for the two detectors with a 4-mm object and 0.5-mm scanning slit. The image is taken from Ref. 21.....	26
2.8 Ghost imaging of (a) 4-mm and (b) 2-mm slits. The blue circles are the data that constitute the ghost imaging and the red triangles are direct imaging measurements by using a scanning slit behind the object. The direct imaging measurements are taken with ~ 106 counts per slit position and scaled to the peaks of the ghost images. The solid lines are guides for the eye. The image is taken from Ref. 21.....	26
2.9 Experimental setup at P09 beamline at PETRA III Synchrotron. The incident beam at 21 keV illuminates the PDC crystal. The HOPG crystal is placed on an optical path of one of the generated PDC photons. The other optical path is free and its photon triggers the AND unit.....	27
2.10 Number of detections per Trigger event. Number of detections for each one of the two detectors (Transmitted and Reflected) per each Trigger detection. (a) Before applying the energy filter, (b) after the energy filter.....	28
3.1 Calculated nonlinear current density including the interactions with bulk plasmons. The spectral features are discussed in the text and transcribed in Table I.....	32
3.2 Phase-matching scheme where the indices p, s, and i stand for the pump, the signal, and the idler respectively. The dashed line indicates the Bragg diffraction condition for the incident beam. (b) Experimental setup. The SR	

illuminates a diamond crystal under phase-matching conditions. The PDC signal is collected by a bent crystal analyzer, which images the beam at the selected energy onto a two-dimensional detector.....	33
3.3 Rocking curves of the x-ray PDC signal for corresponding idler photon energies at 25 eV, 28 eV, 30 eV, and 32 eV. The dashed lines are guide for the eye. The inset shows the comparison between the measured centers of the PDC rocking curves and offset from Bragg predicted by the simulations.....	34
3.4 Rocking curves of the x-ray PDC signal for corresponding idler photon energies at 25 eV, 28 eV, 30 eV, and 32 eV. The dashed lines are guide for the eye.....	36
3.5 Energy (a) and momentum (b) dependence of the 3-dimensional Lindhard functions χ_3. Both momenta and energies are expressed in terms of the Fermi momentum k_F, and the Fermi energy $E_F = \frac{\hbar^2 k_F^2}{2m}$ [69].....	39
3.6 Examples of rocking curves from the aluminum crystal for the idler energy of 19 eV for two reciprocal lattice vectors corresponding to (a) Al(200) and (b) Al(400).....	40
3.7 Spectral dependence of the x-ray into UV PDC process for Al(200) (a) and Al(400) (b) reciprocal lattice vectors respectively.....	41
3.8 (a) Phase-matching scheme. The indices k_p, k_s, and k_i are the k-vectors of the pump, signal, and idler respectively. G is the reciprocal lattice vector. k_b is the k-vector of the Bragg diffraction. (b) Experimental setup.....	44
3.9 Fluorescence measurement in LiF a) without the analyzer and b) with the analyzer.....	47
3.10 Signal count rate as a function of the deviation from phase matching for (a) diamond and (b) and (c) LiF. (b) and (c) correspond to two solutions of the phase-matching equation, with a larger and a smaller angle in accord with the Bragg angle, respectively. The idler energies are 30 and 40 eV for diamond and LiF measurements respectively. The zero on the abscissa corresponds to the phase-matching condition. Dots with error bars are the experimental	

measurements; the solid lines are theoretical simulations. The PDC curves are the board curves. The strong sharp peaks are due to the Bragg reflection. The theoretical calculations for LiF are multiplied by a factor of 5.48

3.11 Signal count rate versus the analyzer detuning from the pump energy for different phase-matching conditions of (a) diamond and (b) LiF. The zero on the abscissa axis is the pump energy. In (a) the legend represents the idler energy. The inset shows the scan where the diamond is at the Bragg condition. (b) Analyzer scan at phase matching for idler energy of 40 eV and offset from the Bragg angle of 5 mrad. The inset (i) shows the scan at the Bragg condition. Insets (ii) and inset (iii) show features of the spectrum, which are discussed in the text.....50

3.12 Spectral dependence of the efficiency of PDC process in LiF. The vertical black solid lines correspond to the L_I edge of the neutral fluorine atom and the K edge of neutral lithium atom.....51

List of Tables

I	Nonlinear resonances and the corresponding transitions.....	42
----------	---	----

List of Acronyms and Abbreviations

ARPES – Angle-resolved photoemission spectroscopy

DFT – Density functional theory

EELS – Electron energy loss spectroscopy

GI – Ghost imaging

HOPG – Highly oriented pyrolytic graphite

PDC – Parametric down-conversion

RIXS – Resonant inelastic scattering

SDD – Silicon drift detector

SNR – Signal-to-noise ratio

SR – Synchrotron radiation

UV – Ultraviolet

XFEL – X-ray free electron laser

XRD – X-ray diffractometer

Abstract

During my Ph.D. I performed a study on different aspects of applications of the effect of parametric down-conversion (PDC) of x-rays. In this thesis I describe the two parts of my work which are dedicated to different regimes of x-ray PDC: x-ray into x-ray PDC and x-ray into ultraviolet (UV) PDC.

Our knowledge, both the theoretical and the experimental, of nonlinear x-ray optics is quite limited in contrast to the visible region of electromagnetic spectrum where the impact of nonlinear optics is hard to overestimate. The reason is mainly the very small efficiency of nonlinear processes in x-ray region, e.g., the second order nonlinear susceptibility, depending on the regime, is about 7-10 orders of magnitude smaller than that in the region of visible light. These days, the availability of strong x-ray sources such as the 3rd generation of synchrotrons and the x-ray free electron lasers (XFEL) allows to extend the experimental studies to x-ray nonlinear optics. One of the most intriguing and basic second order processes is PDC of x-rays.

PDC is a second order nonlinear process where a pump photon interacts with the vacuum field via the nonlinear medium, which leads to the generation of two photons that are commonly called signal and idler. PDC in optical regime is a well-known phenomenon and has been used routinely in the past decades as a source of non-classical states of light, whereas x-ray PDC remains a rather unexplored field. The process is interesting by itself as a part of the field of nonlinear x-ray optics, also it has important application as a probe of valence electron charge density.

The first part of my work is dedicated to the x-ray into x-ray PDC process. Similarly to the optical regime x-ray into x-ray PDC can be used as a source of non-classical states of light in the x-ray portion of electromagnetic spectrum. The importance of this work lies in the interest of the quantum optics experiments in the x-ray regime. The main challenge of obtaining reasonable and thus usable rates of the photon pairs is that when increasing the pump intensity, all sorts of linear scattering processes (elastic, Compton, and fluorescence) also increase and saturate the detectors.

I have described an experimental approach of generating nearly collinear x-ray photon pairs with highly suppressed background noise. To date, the experimental setup I demonstrated became a standard setup for the experiments with x-ray photon pairs.

The second part of my work describes another regime of x-ray PDC, namely x-ray into UV PDC. It has been shown that x-ray into UV PDC can be used to probe electronic properties of materials hence a new spectroscopy method can be developed on the foundation of this process. I describe essential steps towards the comprehensive understanding of the spectra of x-ray into UV PDC:

First, I have provided a theoretical model of the nonlinear optical response of materials that includes a collective phenomenon: bulk plasmons and their interactions with electronic resonances. The model predicts peaks in the spectrum far from any atomic resonances. I have demonstrated experimentally for the first time x-ray into UV PDC spectrum of a diamond crystal that show clear evidence of the interactions with bulk plasmons.

Second, I have reported the first measurement of the x-ray into UV PDC in metals. I have provided spectra from Aluminum crystal that indicate the nonlinear optical response from Fermi energy – another collective electronic effect.

Finally, I have reported on the observation of the x-ray into UV PDC in diamond and LiF using the laboratory x-ray tube source in contrast to the previous experiments that had been done using synchrotron radiation. This part is particularly important since it shows the accessibility of such measurements for the broad physical and chemical community, which, in turn, I believe will excite the interest to the nonlinear x-ray spectroscopy based on x-ray into UV PDC.

Chapter 1

Introduction and background

In recent years, nonlinear optics at x-ray wavelengths have made a decent progress due to the emerging of strong x-ray sources such as 3rd generation synchrotrons and x-ray free electrons lasers (XFELs) [1-3]. Several nonlinear processes such as two-photon absorption [4], sum-frequency generation [5], and second-harmonic generation [6, 7] have been observed. A different-frequency generation experiment has also been proposed [8]. Within the frame of this work, I will mainly focus on another intriguing nonlinear optical effect, namely x-ray parametric down-conversion (PDC).

1.1. Literature review

PDC is a second order nonlinear process in which a pump photon interacts with the vacuum field via the nonlinear medium which leads to the generation of a photon pair: signal and idler. One of the most important applications of PDC in the optical regime is as a source for the generation of non-classical states of light, such as entangled photons and squeezed light [9]. The nonlinearity in the optical region can be described by an anharmonic oscillator. Important to note that the even orders of nonlinearity in the optical regime vanish in centrosymmetric crystals. For x-rays the situation is somewhat different. The process of x-ray PDC was first theoretically described by Freund and Levine in the late 60s [10]. I believe that at this moment it is important to explain the laws of energy and momentum conservation of the process, since I will be addressing to them throughout the entire Thesis. Similarly to the optical regime, the

photons generated during this process must satisfy energy conservation, which can be written as $\hbar\omega_p = \hbar\omega_s + \hbar\omega_i$, where indices p , s , and i represent the pump, the signal, and the idler photons, respectively. The momentum conservation, which usually is called phase matching, cannot be achieved using conventional in nonlinear optics methods, such as periodic polling, birefringence, and rarely, anomalous dispersion. In x-ray wavelengths, at least for low-Z elements, the dispersion is normal, so that $n(\omega_1) > n(\omega_2)$ for $\omega_1 > \omega_2$, where n is the refractive index at a certain frequency. In this case the phase-matching equation in following form $\vec{k}_p = \vec{k}_s + \vec{k}_i$, where k represents the wave vector of the corresponding photon, cannot be met. However, the x-ray wavelengths are comparable to the distances between the atomic planes, thus the phase matching can be achieved by using the reciprocal lattice vector \vec{G} [11]. The phase matching diagram is shown in Fig. 1.1 and the phase-matching equation can be expressed as

$$\vec{k}_p + \vec{G} = \vec{k}_s + \vec{k}_i. \quad (1.1)$$

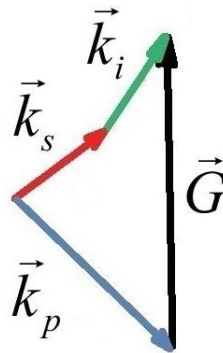


Figure 1.1 - x-ray PDC phase-matching scheme. The indices p , s , and i represent the pump, the signal, and the idler, respectively, G is the reciprocal lattice vector.

The important conclusion to which Freund and Levine came is that the nonlinear optical response of x-rays originates mostly from free-electron properties (plasma-like nonlinearity) in materials rather than inversion asymmetry of a crystal thus is observable even in centrosymmetric crystals.

1.1.1. X-ray into x-ray PDC

Inspired by Freund and Levine proposal, Eisenberger and McCall in 1971 performed and reported an experiment in which they observed parametric conversion of x-ray photons [12]. The authors note that the nonlinearity coefficients at x-ray wavelengths are compensated by a large number of vacuum fluctuations which grows with frequency as ω^3 . They used an x-ray tube with a Molybdenum anode. Utilizing characteristic $K\alpha 1$ line at ~ 17 keV and a Beryllium crystal as a nonlinear medium. The two detectors were placed in accord with the phase-matching equation and coincidence electronics analyzed the detectors signals. The authors observed x-ray photon pairs at about 8.5 keV at their coincidence spectrum. The input flux was about $2 \cdot 10^7$ photons/sec. They report a rate of photon pairs about 1 pair per hour. Such low signal rate, mostly due to the lack of strong x-ray sources at the moment, casted doubt on such further experiments. Nevertheless, the importance of their work is not to be underestimated. Eisenberger and McCall designed a principally typical experimental setup, pointed that the x-ray PDC pairs should be observed in coincidence spectrum due to the strong linear processes such as Compton scattering and elastic Bragg diffraction. Moreover, the energy discrimination is to be applied in order to filter out residual Compton coincidence rate $R_{cc} = R_{D1}R_{D2}\tau$, where R_{D1} and R_{D2} are Compton rate at each one of the two detectors, and τ is the coincidence time window which was 52 nsec for the current experiment. For example R_{cc} in this experiment was about 0.3 pairs/sec whereas x-ray PDC coincidence rate was 4 orders of magnitude lower. Only in 1998 Yoda *et al.* reported the first x-ray into x-ray PDC experiment using synchrotron radiation (SR) [13]. They used a single diamond crystal as a nonlinear medium and observed a coincidence rate of about 6 pairs per hour. Later, in the years 1998-2003, Adams and colleagues conducted a series of experiments and improved the coincidence rate to about 1 pair per 13 seconds [14].

Rapid development of x-ray sources, such as SR sources and XFELs, offer the possibility of extending the quantum optics concepts developed in the visible region of the electromagnetic spectrum [9] to x-ray wavelengths. Paving the way to the further x-ray quantum optics experiments, Shwartz and Harris in 2011 proposed a theoretical model, describing the generation of the Bell states using the process of x-ray into x-ray PDC [15]. Analyzing the plasma-like nonlinearity under the phase-matching

conditions, they show the selection rules of obtaining each of the four Bell states. In the case of degeneracy (when $\hbar\omega_s = \hbar\omega_i$), only two of the four Bell states can be created. Moreover, in this situation the restriction on the polarization of the pumping beam is also applied, namely the polarization of the input beam must be out of the scattering plane. When working off of the degenerate frequency, all of the four Bell states may be generated by choosing the angle of incidence of the pumping beam and its polarization can be either in, or out, of the scattering plane. In 2012 Shwartz *et al.* reported an experiment in which they improved signal-to-noise ratio (SNR) by an order of magnitude by working in transmission (Laue) geometry rather than in reflection (Bragg) with respect to the previous report [16]. Another important result of this work is that the authors demonstrate that in the presence of loss, inherent in x-ray regime due to photoionization, theories based on the Heisenberg picture [17-19] become incorrect, and the appropriate Langevin term must be included into the wave equations. The authors find an agreement between the experiment and the Heisenberg-Langevin equations. The essential improvement of the experimental setup in x-ray into x-ray PDC was made by our group in 2016 [20]. By utilizing the polarization properties of the elastic and nonlinear processes, we show how to suppress the background noise to its minimal values. Important to note that we observed the PDC pairs without any energy discrimination. The angular separation between the generated photons is about 2 degrees which makes them nearly collinear. This work is a part of the current thesis and will be described in details in **Chapter 2**. I would like to note that the proposed geometry became standard in the experiments utilizing x-ray photon pairs [21-23]. In Ref. 21 the first application of x-ray photon pairs is presented. The authors utilized the anti-correlation properties of the k-vectors of the generated photons to image an object. In Ref. 22 the quantum nature of the generated pairs is shown, the authors demonstrate the sub-Poissonian distribution of the detected pairs. I note, that before that work the quantum nature of the generated pairs had not been demonstrated. Moreover, the comparison between the thermal radiation source and quantum radiation source based on x-ray PDC shows large advantage of the quantum approach in case of imaging application. In Ref. 23 the authors demonstrate the single-photon nature of Bragg diffraction process using the x-ray PDC as a source of correlated photons and a highly oriented pyrolytic graphite (HOPG) crystal as a beam splitter.

1.1.2. Nonlinear x-ray spectroscopy

As was mentioned above, PDC is a process that incorporates the vacuum field at the signal and idler frequency as a source of the outcome photons. Since in vacuum the entire spectrum of electromagnetic frequencies is presented, the generation of any pair of photons, as long as they satisfy the phase matching, is possible. This makes x-ray PDC a base for a novel spectroscopy method. We can divide the effect into three regimes with respect to the frequency of the idler photon: x-ray into x-ray, x-ray into ultraviolet (UV), and x-ray into visible PDC. Each one of the processes is different in terms of experimental observations and the properties of material that they reveal. The relevant parameter of x-ray into x-ray PDC is the structure factor of total electron charge density [10, 12], x-ray into UV PDC reveals the charge density of the valence electrons [24], and x-ray into visible provides information about charge redistribution under the optical (visible) field [25, 26]. The nonlinear interactions between x rays and longer wavelengths are particularly interesting, since they present novel physics involving fundamental aspects of light-matter interaction. The main focus of this part of the thesis will be at the x-ray into UV PDC. However, it is extremely important to provide a brief excursion into the x-ray into visible PDC studies. This regime can shed light on the microscopic structure of an optical response of materials. Despite all the progress made in the optical science, our knowledge of the optical properties of materials remains rather limited. All the available measurements provided only macroscopic information due to the limited spatial resolution. Deeper understanding of the optical response, including that on the microscopic level, is necessary, since the optical methods are extremely powerful tools in vast range of studies.

The effects of x-ray and visible sum frequency generation (SFG) and x-ray into visible PDC were first theoretically described in the early 70s [25, 26]. They are akin processes in the sense that they govern the same nonlinear coefficients. Intuitively, they can be viewed as nonlinear x-ray diffraction from optically induced charge density. The x-ray photons is being scattered from the material exposed to an optical field and the energy of the scattered photon is shifted by the energy of the optical field. From those early works, one can extract the main idea of the method. The linear optical susceptibility $\chi^{(1)}(\vec{r})$ is incorporated in the second order nonlinear susceptibility $\chi^{(2)}(\vec{r})$, and similarly to the conventional Bragg diffraction, we measure the Fourier

coefficients of the second-order susceptibility $\chi_G^{(2)}(\vec{r})$, where G is the appropriate reciprocal lattice vector. The observation of the effects, however, is very challenging.

The observation of the effect of x-ray and optical SFG was reported only in 2012 by Glover *et al.* [27]. They used an XFEL at 8 keV and an optical laser at 1.55 eV (800 nm) pulses from a Ti-Sapphire laser. The reciprocal lattice vector C(111) of a diamond crystal was used for the phase matching. They filter out the output x-ray signal by using a crystal analyzer. At the expected energy of 8.0016 keV the authors found a prominent peak that corresponds to the SFG signal which is shown in Fig. 1.2. Another observation that the authors made is the polarization properties of the process. When the polarization of an optical beam is in the diffraction plane (P-polarization) the signal is maximal, whereas when the polarization is normal to the diffraction plane (S-polarization), the signal becomes nearly zero. Despite the success of this experiment, there is a big challenge with the application of this process for material studies – the low efficiency of the process. The effect depends linearly on the intensity of the input optical laser. Most of the times, the optical intensities that are required for the observation of the SFG are larger than the radiation damage threshold of most materials. Another limitation of this process is that the SFG can be observed only in transparent for an optical laser materials and thus cannot be applied for a large class of media e.g. metals.

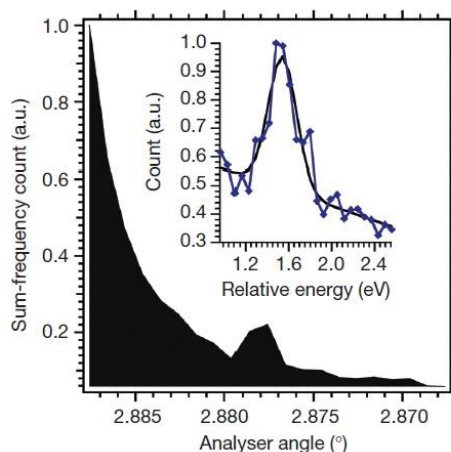


Figure 1.2 SFG signal energy versus analyzer angle. Inset shows energy relative to the x-ray pump at 8 keV. Black line represents the Gaussian fit. The image is taken from Ref. 27.

Another nonlinear process that allows to measure the same nonlinear coefficients is x-ray into visible PDC. This process does not require the sample to be transparent for visible radiation since the visible photon is generated during the process already inside the crystal where the pump beam interacts with the crystal. Since the photons are generated in pairs during the PDC process, we know that by measuring the x-ray signal photons, the visible idler photon was generated also. Most of the times it is not possible to detect the visible or UV idler photon due to the strong visible fluorescence or high absorption inside the material. The observation of x-ray into visible PDC is challenging for the following reasons: the photon energies of the generated x-ray signal differ by only a few eV from the photon energy of the pump and the photons are generated almost into the same direction as the Bragg diffraction due to the phase-matching considerations. This requires a highly collimated and monochromatic input beam and a careful design of the experimental setup. In 2017 Schori *et al.* reported an observation of x-ray into visible PDC using SR. The signals corresponding to the idler energies in the range 280-650 nm were measured. The authors found a reasonable agreement between the experimental results, SFG results, and the theory [28].

Since most of the valence electronic resonances of materials are in the UV range, the process of x-ray into UV PDC becomes of a great interest as a foundation for a novel x-ray spectroscopy technique. The first proposal to probe valence electron density by x-ray into UV PDC was made by Freund in 1972 [29]. Freund has shown that when the idler energy is comparable to the binding energy of valence electrons, the contribution to the nonlinear response from the valence electron charge density is dominant. About a decade later, Danino and Freund reported an observation of x-ray into UV PDC using a laboratory x-ray tube [30]. The authors used a Cu $K\alpha 1$ beam as a pump further monochromatized by a long channeled Ge crystal. The (200) reflection of a LiF crystal was chosen to achieve the phase-matching conditions. The signal that corresponds to the idler energy of 335 eV was observed. The major challenge they had faced is filtering the signal from parasitic radiation. They used a Cobalt filter with K -absorption edge at 7.71 keV to filter out the elastic and Compton scattering. The separation of the signal beam and the tail of the elastic is done by rocking the crystal (rocking curve). Only in 2007 the observation of the effect using SR was reported by Tamasaku and Ishikawa [31]. They used a C(111) reflection of a diamond crystal for

the phase matching and the idler energy of 100 eV. In that work the authors used a NaI scintillation counter and a bent crystal analyzer tuned to the $\hbar\omega_p - 100$ eV in order to filter out the Compton and elastic scattering. Very interestingly that on the rocking curve there was not only a peak that corresponds to the PDC signal but also a dip. The authors interpreted this shape as a Fano interference between Compton scattering and x-ray PDC where the Compton mechanism plays a role of a continuum excitation and x-ray into UV PDC is the discrete excitation [32]. The authors note, however, that the nature of this shape is an open question. Looking ahead, I must say that during my experiments on x-ray into UV PDC I did not observe such a shape. The explanation is that the idler energies that Tamasaku and his colleagues were working in laid on the Compton tail whereas the region of interest of this work is much closer spectrally to the elastic beam.

Investigating the effect further, Tamasaku and his colleagues extracted the nonlinear second-order susceptibility from the Fano shaped rocking curves and reported the first spectrum of x-ray into UV PDC in 2009 [33]. When the idler energy lies well below K -absorption edge of carbon at 289 eV, the line shape is Lorentzian. When idler approaches the edge, the rocking curve becomes asymmetric, and above the absorption edge there is a dip on the rocking curve rather than a peak. When approaching 310 eV idler energy, the rocking curves become asymmetric again. All the rocking curves fit to the Fano formula [32], and the second order nonlinear susceptibility is extracted. The obtained spectrum shows a prominent enhancement of the nonlinear susceptibility near the K -absorption edge which contradicts early theoretical study [34]. The authors also briefly mention that the resonant behavior of the nonlinear susceptibility is observed for a different reciprocal lattice vector of a diamond C(111) and also for another material: silicon with the reciprocal lattice vector Si(111) at the $L_{2,3}$ -absorption edge (around 100 eV) and not at the L_1 -absorption edge probably due to the selection rules. Later, in 2016 Barbiellini and collaborators derive a theory of a renormalization term near the absorption edges using the first principle calculations [35]. They provide the explanation of the effects observed in Ref. 34. The authors come to a conclusion that when the atomic scattering factor f_1 becomes negative, one should expect a resonant behavior of the nonlinear susceptibility in this energy range. They emphasize that the atomic scattering factor f_1 should be calculated for solids because it is different from that calculated for free atoms.

Now let us recall another extremely important property that the effect of x-ray PDC possesses. As I mentioned above, the effect provides **microscopic** information about optical response of materials. The conventional Bragg diffraction which probes the G -th Fourier component of the linear susceptibility $\chi_G^{(1)}$, where G is the corresponding reciprocal lattice vector. The linear susceptibility, in turn, is proportional to the electron charge density, and by measuring the reflection from many reciprocal lattice vector, one can reconstruct the real-space charge density using Fourier-synthesis methods. Similarly to that during the x-ray PDC process, one probes nonlinear susceptibility $\chi_G^{(2)}$ which incorporates the linear susceptibility $\chi_G^{(1)}$. Specifically in the x-ray into UV PDC, the linear susceptibility is proportional to the valence electron charge density [29]. This allows to reconstruct the real-space valence charge density distribution. As a perfect illustration of this idea, well-known Kenji Tamasaku and his team in 2011 published a truly remarkable work [36]. In Fig. 1.2 the reconstructed real-space linear susceptibility at 60 eV is presented with a cut along the 110-plane. Carbon

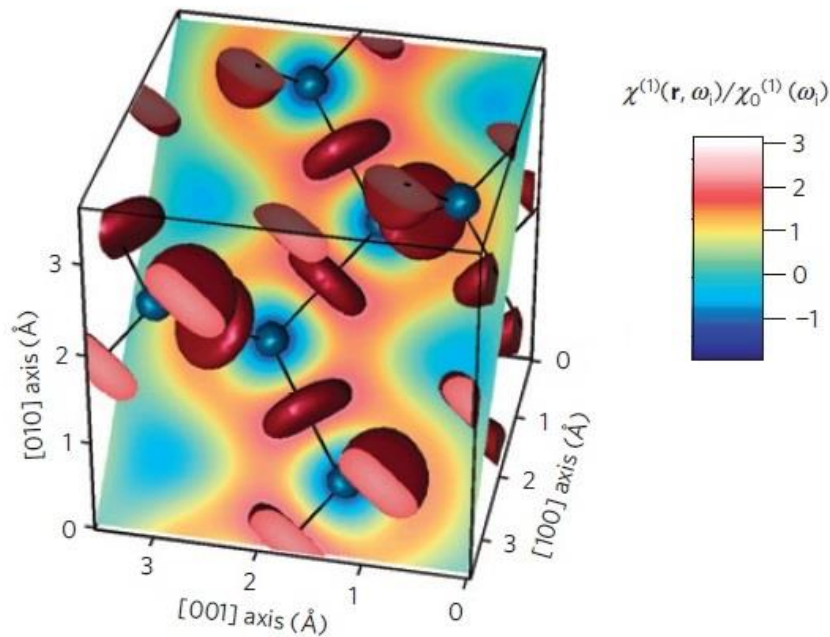


Figure 1.3 Three-dimensional view of normalized linear susceptibility at 60 eV idler energy. Carbon atoms are in the blue spheres, solid lines represent the binding electrons. The image is taken from Ref. 36.

atoms are located at the center of blue spheres. The average linear susceptibility $\chi_0^{(1)}(\omega_i)$ is negative. Thus, the blue spheres respond to light in phase whereas the red

discs in the opposite phase. Interestingly that the red areas have greater contribution to the optical response than the blue areas.

The resolution achieved in this work is $\lambda/380$. Further studies on x-ray into UV PDC will be detailed in **Chapter 3** as they are part of this thesis. The extension of the method on the collective phenomenon such as plasmons [37] and Fermi energy [38] will be discussed in Sections 3.1 and 3.2 respectively. Section 3.3 will be dedicated to the significant improvement of the results obtained using a laboratory x-ray tube source showing feasibility of performing nonlinear spectroscopy measurements in a lab environment.

X-ray into UV PDC has already shown a great potential to become a powerful tool to study electronic properties of materials. The technique can supplement the arsenal of methods of material science and solid state physics. In some cases, x-ray into UV PDC has advantages over the conventional methods based on the analysis of emitted photoelectrons (Angle-Resolved photoemission spectroscopy - ARPES) [40], Auger electrons [41], and characteristic losses of the energy of the electrons (Electron energy loss spectroscopy - EELS) [42]. X-ray into UV PDC does not require vacuum in the volume of the sample and the detectors and expensive electron detection systems. Also unlike conventional x-ray methods based on inelastic x-ray scattering, resonant and non-resonant [43], x-ray into UV PDC provides a direct probe of properties of valence electrons and atomic-scale spatial resolution simultaneously.

1.2. Two coupled wave equations

The generation of a photon pair during the x-ray PDC process can be described by the two coupled wave equations that include losses [16]. The standard method to describe quantum systems that exhibit loss is an introduction of an appropriate Langevin term into the picture [44, 45]. The coupled wave equations are written under slowly varying envelope approximation (SVEA) and undepleted pump approximation:

$$\frac{\partial a_s}{\partial z} + \frac{\alpha_s}{\cos \theta_s} a_s = \kappa' a_i^+ \exp(i\Delta k_z z) + \sqrt{\frac{2\alpha_s}{\cos \theta_s}} f_s, \quad (1.2.1 \text{ a})$$

$$\frac{\partial a_i^+}{\partial z} + \frac{\alpha_i}{\cos \theta_i} a_i^+ = \kappa'^* a_s \exp(-i\Delta k_z z) + \sqrt{\frac{2\alpha_i}{\cos \theta_i}} f_i^+, \quad (1.2.1 \text{ b})$$

where a_s, a_i are the signal and the idler annihilation operators with the commutation relation

$$\begin{aligned} [a_j(z_1, \mathbf{q}_1, \omega_1), a_k^+(z_2, \mathbf{q}_2, \omega_2)] &= \\ &= \frac{1}{(2\pi)^3} \delta_{j,k} \delta(z_1 - z_2) \delta(\mathbf{q}_1 - \mathbf{q}_2) \delta(\omega_1 - \omega_2), \end{aligned} \quad (1.2.2)$$

the angles θ_s, θ_i are the signal and the idler angles taken from the solution of the phase matching equation (1.1), α_s, α_i are the absorption coefficients at the signal and idler

frequency respectively and $\kappa' = \frac{i\kappa}{\sqrt{\cos \theta_s \cos \theta_i}}$, where κ is the nonlinear coupling

coefficient. $\Delta k_z = k_p \cos \theta_p - k_s \cos \theta_s - k_i \cos \theta_i$ is the phase mismatch. We assume that in the directions x, y phase matching conditions are preserved, k_j is a wave vector of the corresponding photon. The terms f_s, f_i are the Langevin noise operators that satisfy commutation relation

$$\begin{aligned} [f_j(z, \mathbf{q}, \omega), f_k^+(z', \mathbf{q}', \omega')] &= \\ &= \frac{1}{(2\pi)^3} \delta_{j,k} \delta(z - z') \delta(\mathbf{q} - \mathbf{q}') \delta(\omega - \omega'), \end{aligned} \quad (1.2.3)$$

where $\mathbf{q}_j = (k_{jx}, k_{jy})$ is the transverse wave vector, k_{jx} and k_{jy} are the wave-vector components parallel to the surfaces of the crystal, z is the direction normal to the surface of the crystal.

The single detector count rate can be calculated via the relation

$R_s = \langle a_s^+(\mathbf{r}, t) a_s(\mathbf{r}, t) \rangle$, the coincidence count rate is

$$R_c = A \iint G(\mathbf{u}, \tau) d\mathbf{u} d\tau,$$

where

$$G(\mathbf{u}, \tau) = \langle a_i^+(\mathbf{r}_2, t_2) a_s^+(\mathbf{r}_1, t_1) a_s(\mathbf{r}_1, t_1) a_i(\mathbf{r}_2, t_2) \rangle. \quad (1.2.4)$$

Here, A is the area of the pump at the input of the nonlinear crystal, $\mathbf{u} = \mathbf{r}_2 - \mathbf{r}_1$, and $\tau = t_2 - t_1$. For details of the solution of the equations (1.2.1) see Appendix A.

1.3. Nonlinear current density

Light-matter interactions may be presented as coupling between Maxwell equation (light) and Newton equation of an electron motion (matter). This is valid if we assume classical particles. This approach shows how the incoming electromagnetic field induces polarization in the material which, in turn, acts as a driving force of the resulting radiation. In this section I discuss the case of x-ray into x-ray PDC and consider the motion of electrons as they were free under the x-ray fields since the energy of x rays is much larger than the binding energies in crystals (correct for low-Z elements). A more general problem when we cannot neglect the binding electron energy is a subject of this thesis and will be detailed in **Chapter 3**.

The linear optical response of materials can be described in terms of polarization under the incoming field $P_i = \varepsilon_0 \chi_{ij}^{(1)} E_j$, where ε_0 is the vacuum permittivity, $\chi_{ij}^{(1)}$ is the linear electric susceptibility tensor, and i and j represent Cartesian components. Note that the Einstein summation convention is applied. When the incoming field is strong enough, the optical response is no longer linear, in this case we must use a general form of the expression for polarization $P_i = \varepsilon_0 (\chi_{ij}^{(1)} E_j + \chi_{ijk}^{(2)} E_j E_k + \chi_{ijkl}^{(3)} E_j E_k E_l + \dots)$, and the nonlinear polarization of interest to us, respectively, will be $P_i^{NL} = \varepsilon_0 \chi_{ijk}^{(2)} E_j E_k$. We will work in terms of nonlinear current density rather than polarization, the relation between them is simply $J_i^{NL} = \dot{P}_i^{NL}$.

In order to find the nonlinear coupling coefficient from the system of equation (1.2.1), we need to calculate the nonlinear current density J_s^{NL} , here the index s represents a signal frequency at which the nonlinear current oscillates. The relation

between them is given by $\kappa = (2\hbar\eta_p\eta_s\eta_i\omega_p\omega_s\omega_i)^{\frac{1}{2}}\epsilon_0 d_{\text{eff}} E_p$, where η_j is the wave impedance at the corresponding frequency, and $d_{\text{eff}} = -\frac{iJ_s^{NL}}{2\epsilon_0\omega_s E_p E_i^*}$ is the effective nonlinear susceptibility. We write the equations of motion of an electron under the driving field and the equation of continuity:

$$\frac{d\vec{v}}{dt} = -\frac{q_e}{m_e}(\vec{E} + \vec{v} \times \vec{B}), \quad (1.3.1 \text{ a})$$

$$\frac{\partial \rho}{\partial t} + \nabla \cdot (\rho \vec{v}) = 0, \quad (1.3.1 \text{ b})$$

where q_e and m_e are the electron charge and mass respectively, $\vec{v}(\vec{r}, t)$ is the velocity field of the electrons, and $\rho(\vec{r}, t)$ is the electron density. Note that in equation (1.3.1 a) the total derivative is used and can be written explicitly via the chain rule using the convective derivative $\frac{d\vec{v}}{dt} = \frac{\partial \vec{v}}{\partial t} + (\vec{v} \cdot \nabla)\vec{v}$. We assume our fields to be plane waves

$\vec{E}_j = \frac{1}{2}(E_0 \exp(i\vec{k}_j \cdot \vec{r} - \omega_j t) + c.c.)$, here the index j represents the corresponding field (pump, signal or idler). Since the electron charge distribution in crystals is periodic, we may use Fourier components of the charge density $\rho_G = \int \rho(\vec{r}) \exp(-i\vec{G} \cdot \vec{r}) dv$, where \vec{G} is the reciprocal lattice vector. Using a perturbation theory approach, one can write the nonlinear current density at the signal frequency ω_s in the following form [12, 46]:

$$\vec{J}^{NL}(\omega_s = \omega_p - \omega_i) = \rho_0 \vec{v}_s^{(2)} + \rho_p^{(1)} \vec{v}_i^{(1)*} + \rho_i^{(1)*} \vec{v}_p^{(1)}, \quad (1.3.2)$$

where $\rho_0, \rho_i^{(1)}, \rho_p^{(1)}$ are the unperturbed and perturbed charge densities at the idler and the pump frequencies respectively, and $v_s^{(2)}, v_p^{(1)}, v_i^{(1)}$ are the velocities at the signal, the pump, and the idler respectively. One can obtain the following expression for the envelope of the nonlinear current density [15]:

$$\begin{aligned}
\mathbf{J}_s^{NL} = & -\frac{q_e \rho_G \omega_s E_p E_i^*}{2m_e^2 \omega_p^2 \omega_s^2 \omega_i^2} [\omega_i \omega_p (\vec{G} \cdot \hat{e}_s)(\hat{e}_p \cdot \hat{e}_i) \\
& -\omega_i \omega_s (\vec{G} \cdot \hat{e}_p)(\hat{e}_i \cdot \hat{e}_s) + \omega_p \omega_s (\vec{G} \cdot \hat{e}_i)(\hat{e}_p \cdot \hat{e}_s)] ,
\end{aligned} \tag{1.3.3}$$

where \hat{e}_j is the polarization vector of the corresponding field. We see three terms that contribute to the nonlinear response: Lorentz force, Doppler current in which the photon at one frequency is inelastically scattered by charge oscillation at another frequency, and displacement of the electrons at one frequency results in the electron sampling a different portion of the field at another frequency.

Chapter 2

X-ray PDC as a source of paired photons

2.1. X-ray photon pairs with highly suppressed background

As was mentioned, one of the most important application of PDC in the optical regime is as a source for the generation of nonclassical states of light, such as entangled photons and squeezed light [9]. The extension of quantum optics into the x-ray regime would open new possibilities for research that would most-likely gain from the existence of commercially available detectors with nearly unity quantum efficiency and with photon-number-resolving capabilities.

2.1.1. Introduction

Although the effect was described theoretically [10] and observed experimentally [12] almost a half of century ago, until this moment, only a few experiments were reported [13, 14, 16]. In recent years several quantum effects in the x-ray regime have been demonstrated, for example, modulation of single γ -photons [47], collective Lamb shift [48], and electromagnetically induced transparency [49]. A method for generating Bell states at x-ray wavelengths by using x-ray into x-ray PDC was proposed in 2011 [15]. However, despite the advantages of PDC over other methods no evidence for such non-classical states of x-ray radiation using PDC has

been reported before this research. There are several major challenges that hamper the use of x-ray PDC as a source for research in the field of quantum optics: 1) the pump photons are Compton scattered into almost any direction. Since the cross section of Compton scattering in a typical experiment is about five orders of magnitude higher than the cross section of PDC, a non-negligible portion of the Compton scattered photons is registered erroneously as PDC photons by the detection electronics. Moreover, Compton scattering limits the input flux to a level at which the Compton scattering rate is much smaller than the inverse of the dead time of the detectors. Thus Compton scattering restricts the enhancement of the rate of x-ray pairs generated via PDC. 2) A large number of quantum optics effects such as the Hong-Ou-Mandel effect [50] and the Bell inequality [51] could be advanced if the emerging generated signal and idler photons were collinear and indistinguishable. However momentum conservation (phase matching) for collinear x-ray PDC is very near the Bragg condition, and since the strength of Bragg scattering is orders of magnitude stronger than the strength of PDC, collinear x-ray photons have never been observed. 3) The bandwidth of x-ray PDC is predicted to be on the order of several kilo electron-Volts [16] while x-ray optical components (except from detectors) have bandwidths narrower than a few hundred electron-Volts.

In this Chapter I will describe an experiment demonstrating how to suppress Compton and Bragg scattering, while increasing the coincidence count rate of the photon pairs that are generated by x-ray PDC, which results in the observation of nearly collinear x-ray photons.

2.1.2. Theoretical basis

As was mentioned in Subsec. 1.1. similarly to the visible regime, in x-ray PDC the pump and the generated photons must satisfy energy conservation, which can be written as $\hbar\omega_p = \hbar\omega_s + \hbar\omega_i$. The indices p , s and i represent the pump, the signal, and the idler respectively. We also recall, that since the x-ray wavelengths are comparable to the distances between the atomic planes, phase matching can be achieved by using the reciprocal lattice vector \vec{G} [11]. The phase matching diagram is shown in Fig.

2.1(a) and the phase matching equation is expressed as $\vec{k}_p + \vec{G} = \vec{k}_s + \vec{k}_i$, where k denotes the wave vector of the corresponding photon.

Because of the weak dispersion in the x-ray regime, the magnitudes of phase matching angles for frequency-degenerate idler and signal are very close to the Bragg angle. Consequently, the phase matching angles for collinear degenerate signal and idler are within the rocking curve of the Bragg diffraction. Since in most cases Bragg scattering is much stronger than PDC, the observation of collinear signal and idler photons requires the suppression of Bragg scattering.

To understand the approach to eliminating Bragg and Compton scattering, we recall the Klein-Nisina formula for the Compton differential cross-section in case of the input photon energy is much smaller than the rest mass of electrons that is 511 keV,

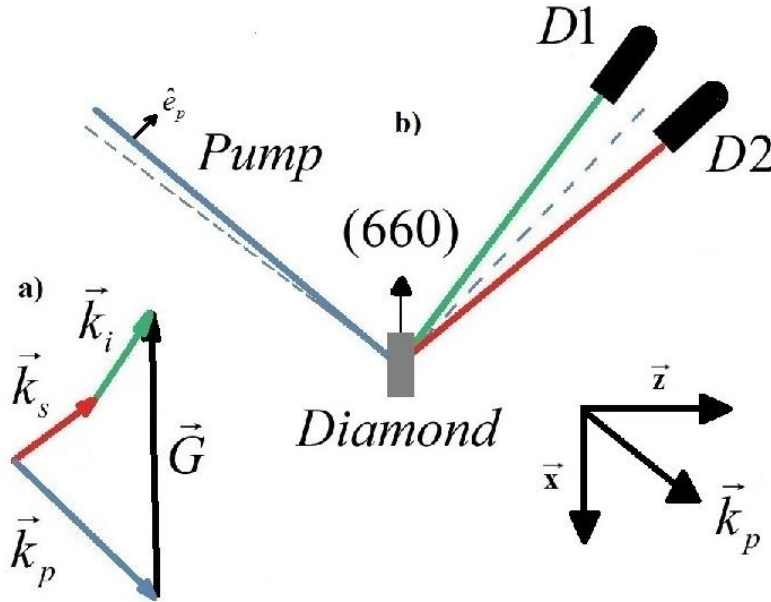


Figure 2.1 (a) Phase-matching scheme. (b) Schematic of the experimental setup. The indices $p, s,$ and i are for the pump, signal, and idler respectively, \vec{G} represents the reciprocal lattice vector orthogonal to the (660) atomic planes and \hat{e} is a polarization vector. D1 and D2 indicate the two detectors.

reduces to the simple Thomson differential cross section (note that we write the formula for polarized light in the scattering plane as illustrated in Fig. 2.1 (b)) [52]:

$$\frac{d\sigma_{Th}}{d\Omega} = r_e^2 \cos^2 \theta, \quad (2.1.1)$$

where θ is the scattering angle, Ω is the solid angle, and the r_e is the classical radius of electron. It is clear that the equation (2.1.1) approaches zero when the scattering angle is 90 degrees. As a result, under these conditions both Compton and Bragg scattering are highly suppressed.

As discussed in Subsec. 1.3., the nonlinearity that dominates at x-ray wavelengths is a plasma-like nonlinearity [12, 46]. A non-uniform charge density distribution and the Lorentz force are the essence of the second order nonlinearity even in centro-symmetric crystals. The nonlinear current density given by the equation (1.3.3) in the geometry when the scattering angle is 90 degrees, assuming that the signal and the idler photon are generated in the same direction, can be approximated to

$$J_s^{NL} = \frac{q\rho_G E_p E_i^*}{2m^2 \omega_p^2 \omega_i} (\vec{G} \cdot \hat{e}_p)(\hat{e}_i \cdot \hat{e}_s). \quad (2.1.2)$$

Comparison of the equations (2.1.1) and (2.1.2) clearly shows us that unlike the cross-sections for Compton and Bragg scattering, the nonlinear current density for pump polarization in the scattering plane and angles between the source and the detector are close to 90 degrees is non-negligible, since the scattered idler and signal (indices i and s respectively) are nearly collinear and the angle between the pump photon and the reciprocal lattice vector is around 45 degrees. Hence under these conditions, we expect to measure x-ray pairs with negligible background. Similar approach was used, for example, in a work demonstrating the effect of nonlinear Compton scattering [53]. We also note that similar to Bragg scattering, the nonlinear scattering is proportional to the Fourier component of the electron density corresponding to the chosen reciprocal lattice vector. However, unlike Bragg scattering it is also proportional to the magnitude of the reciprocal lattice vector. Thus, although, the Fourier component decreases at higher order reflections, the dependence on the reciprocal lattice vector moderates the reduction of the nonlinear current at higher order reflections. Consequently we can choose the pump photon energy to be high enough to reduce the undesired effects of loss.

2.1.3. Experiment

The experiment described here was conducted at beamline ID-10 of the European Synchrotron Radiation Facility. The schematic of the experimental setup is shown in Fig. 2.1 (b). A monochromatic pump beam at a photon energy of 21 keV illuminates a high quality diamond crystal with dimensions of 4 mm × 4 mm × 0.8 mm in transmission (Laue) geometry. We use the reciprocal lattice vector normal to the C(660) atomic planes for phase matching. The angle that satisfies the Bragg condition for those atomic planes is 44.73 degrees. The scattering angle in this case is almost 90 degrees. The generated signal and idler photons are collected by two silicon drift detectors (SDD) with a diameter of 5.6 mm located 800 mm from the crystal. The average input intensity is 2×10^{12} photons/s. We estimate that the polarization ratio between the in-plane and the out-of-plane polarizations of the pump beam is about 10^3 . The coincidence electronics records only photons that hit two detectors within a time window of 370 ns. The coincidence circuit is depicted in Fig. 2.2. Each of the SDDs, when a photon hits the detector, produces a logic signal that then goes into a logic unit AND. Simultaneously, the detectors produce the analog signal from their multi-channel analyzers (MCA) that have energy resolution. When two logic signals hit the AND unit

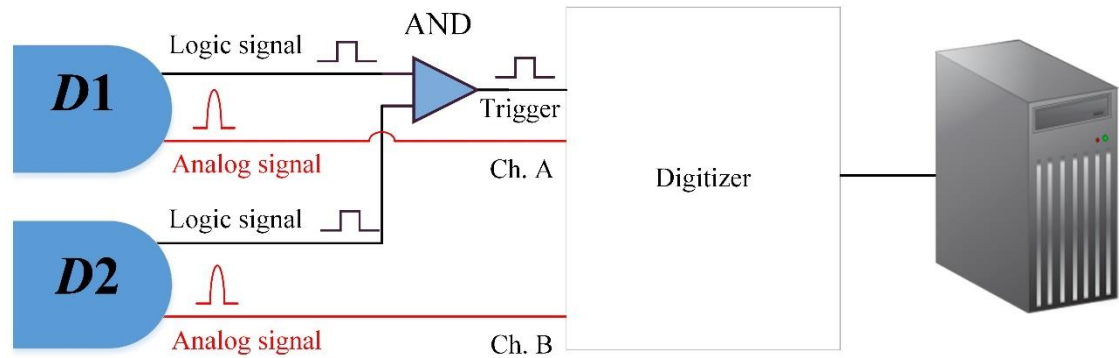


Figure 2.2 Coincidence electronic circuit. The detectors *D1* and *D2* produce logic signals that trigger the logical unit AND. When the coincidence event occurs, the analog signals from detector's multi-channel analyzers are recorded by the digitizer.

within the time window mentioned above, it produces a pulse and triggers the digitizer to record the analog signals. Next, we scan through the data and apply the following rule as a photon energy filter for each of the coincidence events: the sum of the energies from the two detectors equals to the pump energy within an energy window of 500 eV. All experimental data are corrected for air absorption.

In order to estimate the background noise, we measure the detector count rates when the crystal and the detectors are at the phase matching angles. The average total count rate is about $(2.21 \pm 0.05) \times 10^3$ photons/s at detector *D1* and $(2.12 \pm 0.05) \times 10^3$ photons/s at detector *D2*, which agrees with the Thomson cross-section calculation for the current polarization ratio of the beamline. The typical spectrum is shown in Fig. 2.3. The narrow peak on the right is the elastic scattering, the second peak with an energy

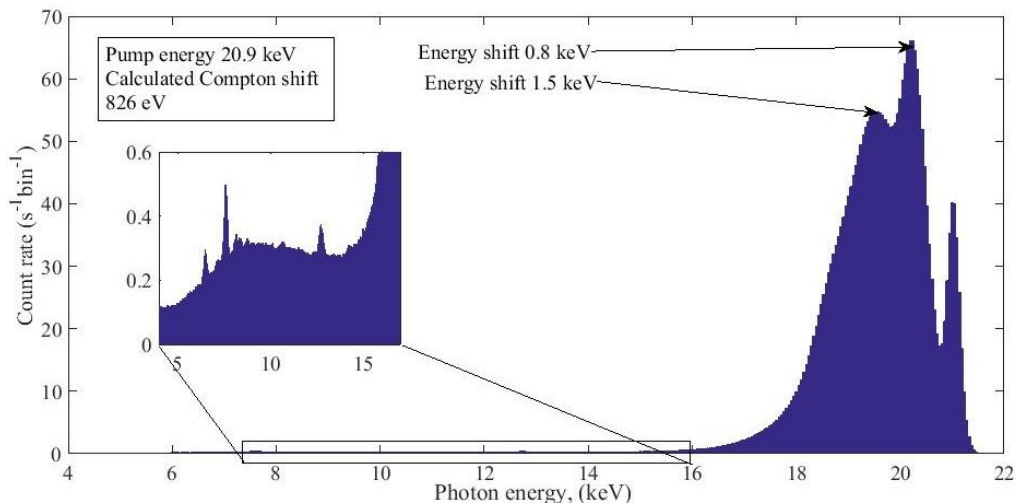


Figure 2.3 Typical raw spectrum measured by a single detector. The Compton peak is at the calculated photon energy. The peak with the energy shift of 1.5 keV from the elastic is the escape peak. The inset shows the structure at the energies of interest. Several fluorescence peaks originated mainly from elements such as iron and lead are clearly seen in the range of 6 keV – 15 keV.

shift of 800 eV is the Compton scattering (the calculated Compton shift is 826 eV). The broad peak with the energy shift of 1.5 keV is so-called the escape peak. This is a well-known artefact of silicon-based detectors. It happens when the photon loses its kinetic energy on the *K*-edge of Silicon in the detector. The inset shows the details of the

spectrum in the area of interest. Fluorescence peaks originated mainly from elements such as iron and lead are present due to the presence of those elements in the experimental hutch. A fast slope in the spectrum around 5 keV is due to the lower efficiency of the detector at those energies. We estimate the energy resolution at 21 keV to be about 400 eV according to the full width at half-maximum (FWHM) of the elastic peak.

2.1.4. Results and discussion

Next, we measure the coincidence count rate. By using a setup where the angles between the source and the detectors are near 90° we reduced the Compton count rate to its minimal values. This allows us to choose the deviation angle of the pump from the Bragg angle to be as small as the FWHM of the rocking curve of the Bragg diffraction and thus increase the PDC count rate. It is important to note that the deviation angle in the present experiment is limited only by the physical dimensions of the detectors, which restricts the possibilities for phase matching.

Energy histograms at the frequency degenerate phase-matching case for the angular separation of 2.3° between the detectors are shown in Fig. 2.4. The degenerate case is defined as $\omega_s = \omega_l = \omega_{s,0}$, where $\hbar\omega_{s,0}$ is the degenerate photon energy. Here, panels (a) and (b) correspond to the first and the second detector respectively. Of importance, even without applying the energy filter described above it is seen that the peaks corresponding to the PDC effect are pronounced. The total count rate obtained 0.149 ± 0.003 pairs/s. The photon energy filter removes the accidental coincidence Compton counts. The PDC count rate after applying the filter is 0.088 ± 0.002 photons/s with a bandwidth of than 1.5 keV at the FWHM. The Heisenberg-Langevin theory described in Subsec. 1.2. predicts a bandwidth of about 3.5 keV at the FWHM and a count rate of 2.6 pair/s.

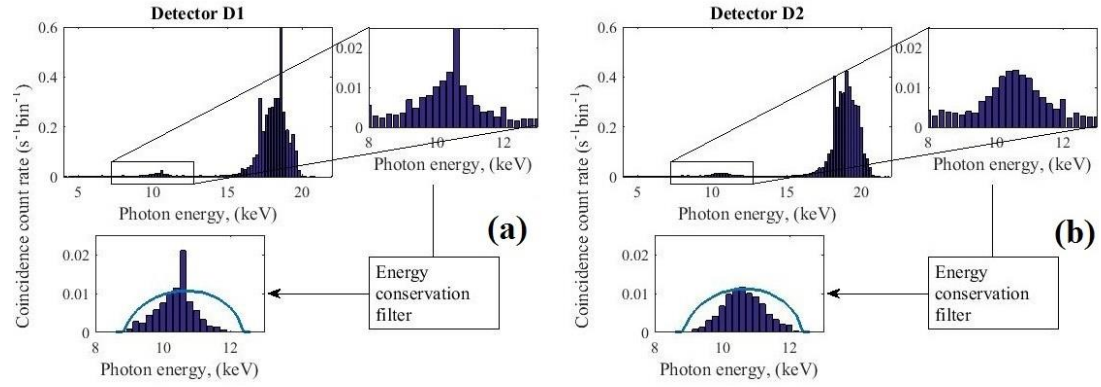


Figure 2.4 Energy histograms of the measured coincidence count rate at the degeneracy for detectors *D1* and *D2* are depicted on a) and b) respectively. Raw coincidence data and results of applying the energy conservation filter, i.e. the sum of the energies of each coincidence event equals to the pump energy within an energy window of 500 eV. Solid lines are theoretical calculations.

If we move the detectors from the degenerate phase-matching position we should observe a corresponding shift in the coincidence spectra. Indeed, Fig. 2.5 shows energy histograms at the off-degenerate phase matching after applying the photon energy filter. Here, panels (a) and (b) correspond to the off-degenerate conditions of $\omega_s / \omega_{s0} = 1.2$ and $\omega_s / \omega_{s0} = 1.4$ respectively. As we move further away from the degeneracy the coincidence count rate drops down. At $\omega_s / \omega_{s0} = 1.2$ we measure 0.058 ± 0.002 pairs/s and at $\omega_s / \omega_{s0} = 1.4$ only 0.012 ± 0.001 pairs/s. In the latter case, the PDC signal is outweighed by the Compton tail and it is observed only with the photon energy filter. The divergence in coincidence count rate between the theory and the experiment is about factor of 20. The model assumes that the pump is a plane wave whereas in reality it has a finite width. In addition, the theory does not take into account the overlap between the pump and the generated beams and the rich temporal structure of the beams. We define the SNR as the ratio between the PDC and the Compton tail count rate at this spectral region. The obtained SNR is 113 for the degenerate energy.

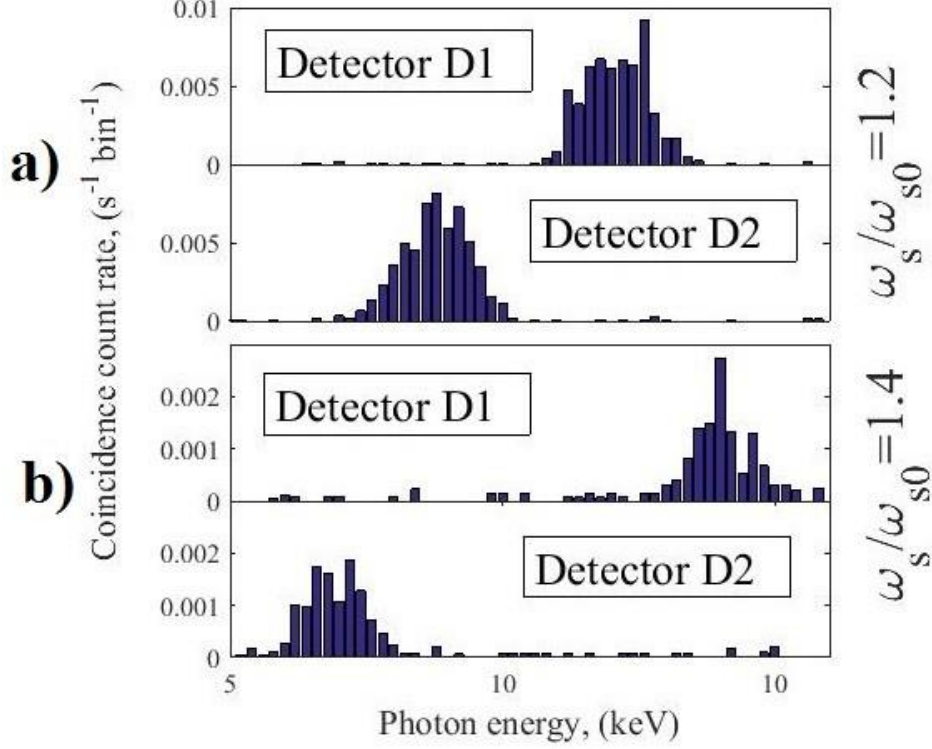


Figure 2.5 Coincidence diagrams after applying the energy conservation filter for the cases off the degeneracy a) $\omega_s / \omega_{s0} = 1.2$ and b) $\omega_s / \omega_{s0} = 1.4$.

In conclusion, we have demonstrated how to generate x-ray photon pairs with negligible background by using a geometry where the angles between the pump and the emerging photons are nearly 90° and the pump polarization is in the scattering plane. The maximum coincidence count rate was about 0.1 pairs/s and the Compton count rate was about 2×10^3 photons/s whereas in the previous work described in Ref. [6] the highest count rate of PDC was 0.025 pairs/s and the Compton count rate is about 2×10^4 photons/s for an input intensity of 2×10^{11} photons/s. Such a significant background suppression allowed us to measure the actual coincidence count rates without any energy discrimination. Consequently, in contrast to all previous reports, in the present work the coincidence count rates at the degeneracy do not depend on the choice of the energy discrimination and the energy histograms we have described in this paper represent the true spectra of the coincidence counts. Our results can be further improved with higher ratio between the polarizations of the input beam. This can be achieved either by using undulators with better polarization ratio or by using x-ray polarizers before the generating crystal. Since by using the geometry we present here Compton scattering

is greatly reduced, the input intensity can be increased substantially without saturating the detectors. Finally, since in the geometry we describe here Bragg scattering is highly suppressed as well, our experiment shows the way to generate collinear indistinguishable x-ray pairs via PDC. This can lead to the observation of quantum optics effects such as the Hong-Ou-Mandel effect with x-rays. It is interesting to note that the theoretical calculation of the coincidence count rate of collinear signal and idler predicts that the temporal width of the biphoton wave function can be shorter than 100 attoseconds. In Fig. 2.6 the calculations of the second-order correlation functions are shown for different phase-matching configurations [54]. This is shorter than any previously discussed biphoton wave functions and it is enabled by the very large pump frequency and the very weak dispersion in the x-ray regime.

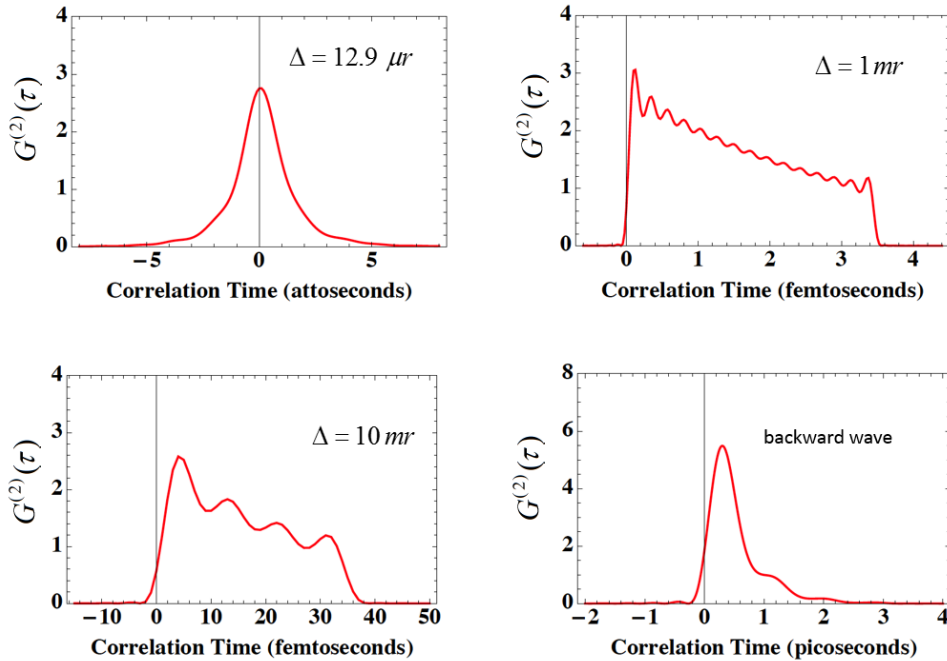


Figure 2.6 Calculation of the second-order correlation function for several phase-matching configurations for the case of degenerate energy. Δ is the offset from the Bragg angle. The correlation time is the smallest when the offset is the smallest, i.e. the generated photons are nearly collinear.

The summary of this project was published in 2016 in a peer review journal Physical Review A [20].

2.2. Joint works

In this Section I would like to describe briefly the experiments, in which I have participated and contributed. The experimental setups are based on the geometry from the previous section.

The first application of x-ray photon pairs was reported by Schori *et al.* [21]. We utilized the 90 degrees geometry developed previously. The idea was to show a ghost imaging (GI) technique with correlated photons. GI utilizes the correlation between two spatially separated beams to retrieve information about an unknown object. In a typical scheme of GI one of the beams interacts with the object and is being collected by a single-pixel detector behind it. The second beam is collected by a detector with spatial resolution. The object is reconstructed by the correlation function between the two detectors since the data from each one of them is insufficient for the imaging. The type of GI where the correlated photons are used is called quantum GI. PDC process commonly plays a role of a source of such correlated photons, at optical wavelengths the scheme is used extensively [55].

We conducted the experiments at the RIKEN SR physics beamline (BL19LXU) of Spring-8 [56]. The arm in which the object and detector without spatial resolution is placed, is called test, whereas the arm without the object and with the spatially resolving detector is called reference. The spatial resolution in the current experiment was achieved by scanning over the detector area with a 0.5 mm slit. The objects were 4-mm and 2-mm slits. Scanning with the slit is effectively moving the detector position so we expected to observe a shift in coincidence PDC spectrum in order to prove that we see the photons generated by x-ray PDC similarly to what is described in Subsec. 2.1.4 (see Fig. 2.5). Indeed, the shift was observed. In Fig. 2.7 we see a coincidence spectra as a function of a position of a reference slit for a 4-mm slit as an object. For 2-mm object the similar spectrum was observed.

Next, we select the photons within a certain bandwidth from the two detectors (in this case we chose the energy around the degenerate energy of 11.5 keV with the bandwidth of 500 eV) and reconstruct the object. In Fig. 2.8 the results of quantum GI

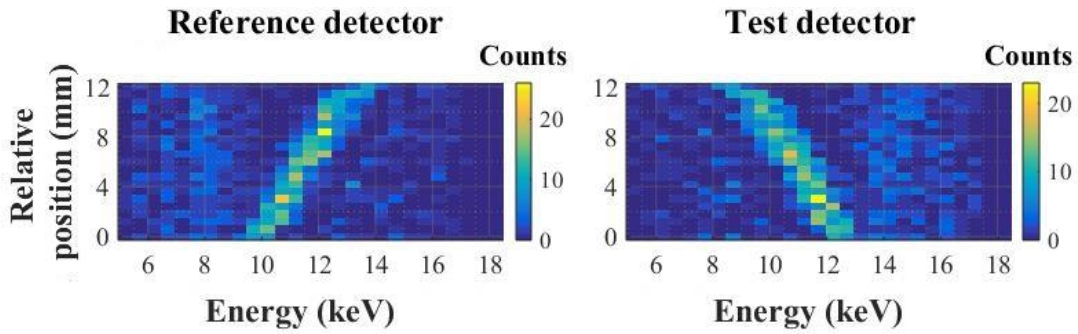


Figure 2.7 Coincidence spectra for the two detectors with a 4-mm object and 0.5-mm scanning slit. The image is taken from Ref. 21.

are shown with comparison to the direct imaging for 4-mm and 2-mm slits. The coincidence count rate in this experiment was about 7 pairs per hour due to the narrow energy bandwidth and small slit size. From the results it is seen that the background level is nominally zero. It is also clear from the results that our experimental scheme is well suited to measurements with extremely low count rates, which can be advantageous for a variety of quantum optics experiments. This is due to the extremely low noise of x-ray detectors and the use of coincidences and the energy resolution of our system.

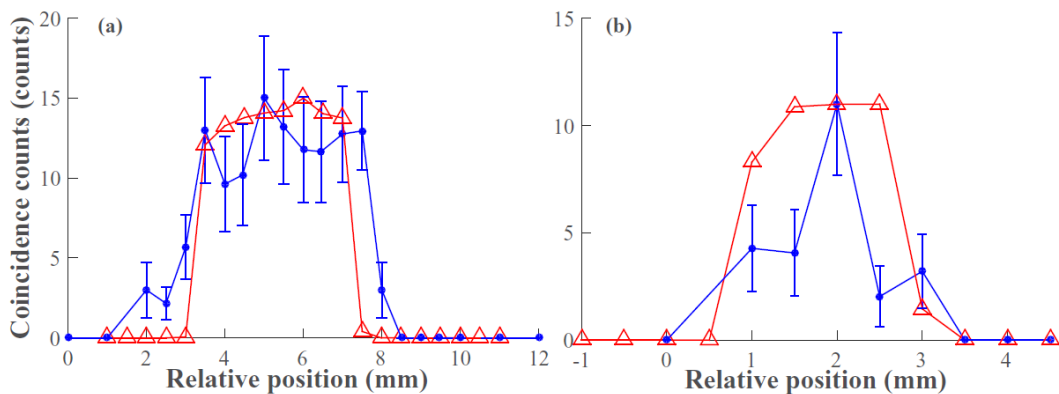


Figure 2.8 Ghost imaging of (a) 4-mm and (b) 2-mm slits. The blue circles are the data that constitute the ghost imaging and the red triangles are direct imaging measurements by using a scanning slit behind the object. The direct imaging measurements are taken with ~ 106 counts per slit position and scaled to the peaks of the ghost images. The solid lines are guides for the eye. The image is taken from Ref. 21.

Another experiment using the same setup that I have participated in was conducted at P09 beamline of PETRA III Synchrotron of DESY [57]. At the moment of submission of this thesis the paper summarizing the results of this experiment is in the preparation. However, I will describe the principal results of the work. The schematic of the experimental setup is depicted in Fig. 2.9. The SR beam hits a diamond crystal under the phase-matching conditions to generate a photon pair via PDC process. One of the photons plays a role of a trigger for the AND unit. On the optical path of the second photon, a beam splitter was placed with two detectors on both exits of the beam splitter (Transmitted and Reflected). The HOPG crystal under Bragg condition for the 10.5 keV beam was used as a beam splitter. We set the coincidence setup for the following logic: $\text{Trigger} \cdot (\text{Transmitted} + \text{Reflected})$, where the dot product means logical AND and plus means logical OR. This experiment is the extension of beam-splitter experiments conducted by Grangier *et al.* [58] into the x-ray region of the electromagnetic spectrum. We observed that the coincidence events are always between the Trigger and Transmitted or Trigger and Reflected and never between Transmitted and Reflected (triple coincidence). This is a proof that x-ray PDC is a source of single photons and not just a low count rate of a classical (thermal) source.

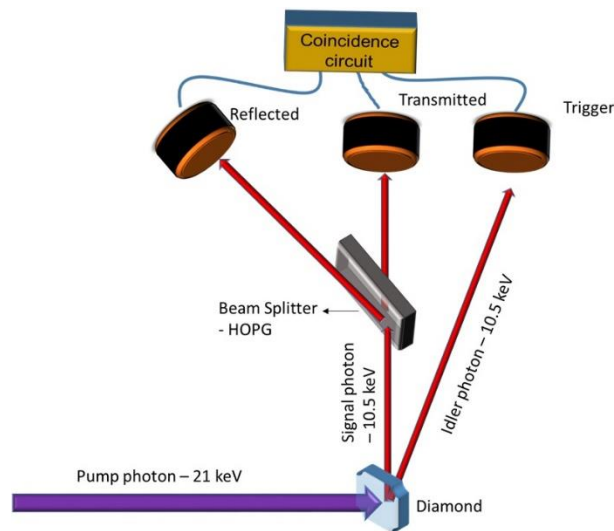


Figure 2.9 Experimental setup at P09 beamline at PETRA III Synchrotron. The incident beam at 21 keV illuminates the PDC crystal. The HOPG crystal is placed on an optical path of one of the generated PDC photons. The other optical path is free and its photon triggers the AND unit.

The experimental results are shown in Fig. 2.10. In Fig. 2.10 (a) the coincidence events before applying the energy filter are shown. We see that triple coincidence events are present (they correspond to the (1, 1) coordinates in the horizontal plane). Those events are the result of erroneously detected coincidence Compton photons. After applying the energy filter, they become strictly zero as shown in Fig.10 (b).

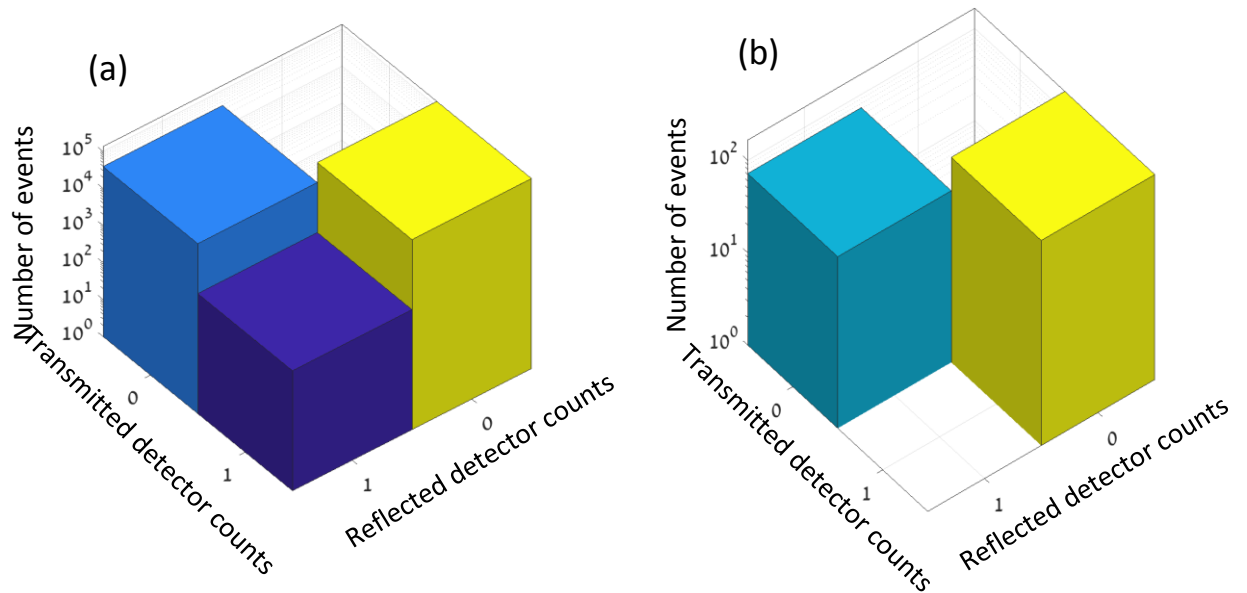


Figure 2.10 Number of detections per Trigger event. Number of detections for each one of the two detectors (Transmitted and Reflected) per each Trigger detection. (a) Before applying the energy filter, (b) after the energy filter.

Chapter 3

Nonlinear x-ray spectroscopy

This Chapter will be dedicated to another intriguing regime of x-ray PDC, namely x-ray into UV PDC. Since most of the characteristic energies of the valence electrons that comprehensively define chemical properties of materials, are in the UV range, this regime of x-ray PDC can be used to probe those electron properties.

3.1. Evidence for collective nonlinear interactions in x ray into UV parametric down-conversion

3.1.1. Introduction

Nonlinear spectroscopy based on the x-ray into UV PDC process has yet a long way to make until it becomes a routine spectroscopy technique in material science and solid-state physics. The number of reports in the literature dedicated to the process is very small comparing to the amount of information available regarding more traditional x-ray spectroscopy methods such as Compton scattering and RIXS. Until this work, the authors of x-ray into UV PDC related papers have considered only local responses [31-33, 35, 36, and 39]. In this Section I extend the study on nonlinear x-ray optics to include the interactions with a collective electron phenomenon, namely bulk plasmons. Looking ahead, I say that the spectrum of x-ray into UV PDC from a Diamond crystal in the energy range shows clear evidence of such interactions predicted by the generalized classical model of nonlinearity that will be developed further.

3.1.2. The model

I start by describing a theory that includes the interactions with plasmons and that predicts the existence of peaks far from atomic resonances (the binding energy of electrons in carbon are 12, 16, and 280 eV). Similarly to Subsec. 1.3. we consider a classical model of nonlinear current density. The nonlinear current density plays a role of a driving term that generates the signal wave. We recall that it can be found as a second order perturbation of electron motion [46]:

$$\vec{J}_s^{NL} = \rho_0 \vec{v}_s^{(2)} + \rho_p^{(1)} \vec{v}_i^{(1)*} + \rho_i^{(1)*} \vec{v}_p^{(1)}, \quad (3.1.1)$$

where ρ_0 is the unperturbed charge density, $\rho_j^{(1)}$ is the charge density modulated by the j -th frequency, and $v_j^{(n)}$ is the n -th order velocity at the j -th frequency. We generalize previously described model for x-ray into UV process. Namely, we do not neglect the restoring force in the equation of motion [27, 46]:

$$\frac{\partial \vec{v}_j}{\partial t} + (\vec{v}_j \cdot \nabla) \vec{v}_j + \omega_0^2 \vec{r}_j = -\frac{q_e}{m_e} (\vec{E}_j + \vec{v}_j \times \vec{B}_j) \quad (3.1.2 \text{ a})$$

$$\frac{\partial \rho_j}{\partial t} + \nabla \cdot (\rho_j \vec{v}_j) = 0, \quad (3.1.2 \text{ b})$$

where m_e is the effective electron mass, q_e is the electron electric charge, B_j is the magnetic field, E_j is the electric field strength of the corresponding wave, and ω_0 denotes the resonance frequency. We assume that the motions of electrons at the signal and pump frequencies are free, since their photon energies are well above any electronic binding energy in the nonlinear medium. At the idler frequency we include the restoring force term, since the idler photon energy is on the order of the binding energy of the valence electrons. We solve the system of equations (3.1.2) together with Maxwell equations. Note that I took the Gauss law in the form $\nabla \cdot \vec{E} = \frac{\rho_j^{(1)}}{\epsilon_0}$ as in Ref. 46, where

ϵ_0 is the vacuum permittivity. For detailed derivation of the nonlinear current density in this case address Appendix B. Here I give the final expression:

$$J_G^{NL}(\omega_s) = \frac{\epsilon_0 q \chi_G^{(1)}(\omega_i) E_i^* E_p}{m^2 \omega_p} \left(- \frac{(\vec{G} \cdot \hat{e}_i)(\hat{e}_p \cdot \hat{e}_s)}{\left(1 + \frac{\omega_{plasma}^2}{(\omega_o^2 - \omega_i^2)}\right)} \right), \quad (3.1.3)$$

where $\chi_G^{(1)}(\omega_i)$ is the Fourier component of the linear electric susceptibility that correspond to the reciprocal lattice vector \vec{G} at the idler frequency, and \hat{e} is the polarization vector of the corresponding wave. I estimate $\chi_G^{(1)}(\omega_i)$ for idler energies below 35 eV from the experimental data [59] and for higher energies I use the values calculated by Henke *et al.* [60]. The plasma resonance $\hbar\omega_{plasma}$ is calculated by using

the well-known expression for the plasma frequency $\omega_{plasma} = \sqrt{\frac{q_e \rho_0}{m_e \epsilon_0}}$, and equals 31

eV for diamond. In our calculations of the nonlinear current density we take the plasma resonance energy of 34 eV due to the dispersion of plasmons in the [110] direction [61].

The expression in equation (3.1.3) predicts a nonlinear resonance at a frequency, which is equal to $\omega_i = \omega_{NL} = \sqrt{\omega_{plasma}^2 + \omega_0^2}$. In Ref. 27 the authors took ω_0 to be equal to the band transition of a diamond crystal for the correction of the nonlinear current density. Since in real crystal there is more than one resonance associated with band transitions, we use the resultant current density in the following form

$$J_{tot}^{NL} = W_1 J_1^{NL} + W_2 J_2^{NL} + \dots, \quad (3.1.4)$$

where W_j are weight coefficients and J_j^{NL} are the nonlinear current densities from the equation (3.1.3) that corresponds to the j -th resonance.

Figure 3.1 shows simulations of the spectrum of the resultant nonlinear current density calculated by using equation (3.1.4). For simplicity I took the weight coefficients to be equal. I include resonances associated with band transitions in a diamond crystal as described in the literature [62, 63]. The simulation shows that the PDC signal depends strongly on the photon energy of the idler when it is near ω_{NL} . Each spectral feature represents nonlinear interactions between the band transitions and bulk plasmons. The properties of the features are shown in Table I. This dependence cannot be explained by any theory that does not include non-local interactions.

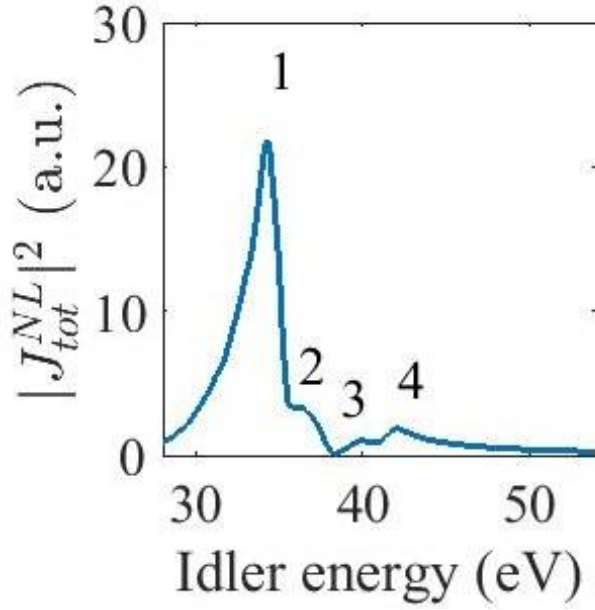


Figure 3.1 Calculated nonlinear current density including the interactions with bulk plasmons. The spectral features are discussed in the text and transcribed in Table I.

I note a recent work by Lucchini and colleagues in which the measurements of absorption on a polycrystalline Diamond sample show the absence of resonant transitions in this photon energy range [64].

TABLE I. Nonlinear resonances and the corresponding transitions.

Feature #	Transition energy, eV	Nonlinear resonance $\hbar\omega_{NL}$, eV
1	5.5 ^a	34.4
	7.4 ^b	34.8
2	12.6 ^b	36.1
	14.4 ^a	36.9
	16 ^b	37.6
3	20 ^b	39.4
4	24 ^b	43.4

^a Ref. 62, ^b Ref. 63.

3.1.3. The experiment and procedure

This experiment was conducted on the GALAXIES beamline at the SOLEIL synchrotron facility [65]. The experimental setup is shown in Fig. 3.2. The input beam

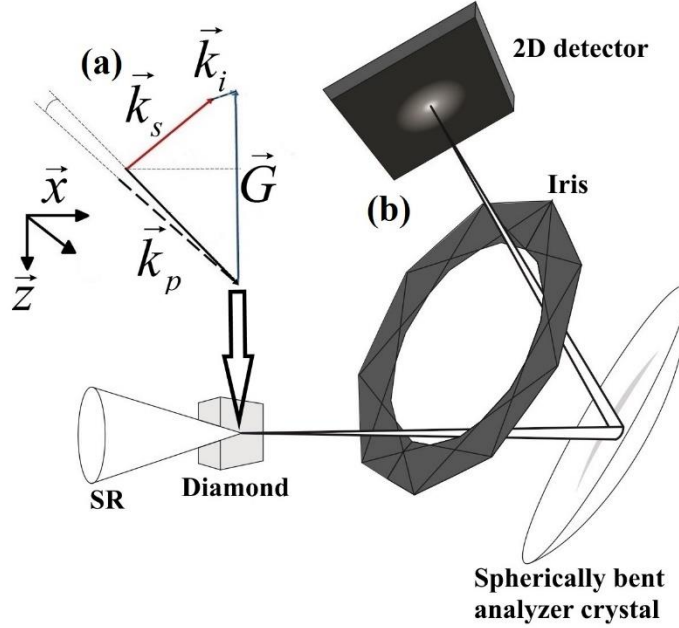


Figure 3.2 (a) Phase-matching scheme where the indices p, s, and i stand for the pump, the signal, and the idler respectively. The dashed line indicates the Bragg diffraction condition for the incident beam. (b) Experimental setup. The SR illuminates a diamond crystal under phase-matching conditions. The PDC signal is collected by a bent crystal analyzer, which images the beam at the selected energy onto a two-dimensional detector.

is a monochromatic beam of 9.995 keV using Si(111) reflection of the beamline double crystal monochromator. We used the reciprocal lattice vector normal to the C(220) atomic planes of a Diamond crystal for the phase matching in reflection (Bragg) geometry. We select the photon energy of the signal by using the beamline Rowland circle RIXS spectrometer. The instrument consists of a spherically bent Si(555) crystal analyzer with a curvature radius of one meter and a hybrid-type pixelated 2D MERLIN detector. We estimate that the photon energy resolution of the receiving optics is about 0.5 eV. In order to reduce the background radiation along with spatial filtering of the

detector image, we placed an adjustable iris in front of the analyzer as depicted in Fig. 3.2 (b). Typical iris diameter during the measurements was about 5 mm.

The first experimental step is to verify that we observe PDC by confirming that the phase-matching conditions are satisfied. We measure the rocking curves of the x-ray signal that correspond to various idler energy. Examples of such measurements are shown in Fig. 3.3. The peak positions of the rocking curves are slightly shifted by about 0.01 degrees from the solutions of the kinematic phase-matching equation as one can see also in the simulations. The simulations are based on the calculation of a single detector count rate as described in Subsec. 1.2. The reason for that shift is that the rocking curves include a large number of the vacuum fluctuations modes with different

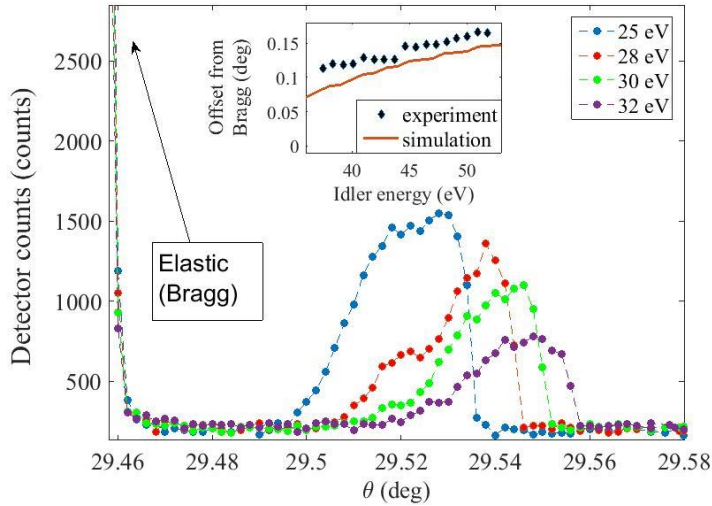


Figure 3.3 Rocking curves of the x-ray PDC signal for corresponding idler photon energies at 25 eV, 28 eV, 30 eV, and 32 eV. The dashed lines are guide for the eye. The inset shows the comparison between the measured centers of the PDC rocking curves and offset from Bragg predicted by the simulations.

weights that are determined by the strength of the nonlinearity and the boundary conditions at the various modes [39]. The inset in Fig. 3.3 shows the comparison between the experimentally observed peaks and those obtained in the simulations. The difference between the estimated offset from Bragg and measured peaks is about 0.01 deg. We note that this difference is smaller than the width of the curves (about 0.02-

0.03 degrees). The phase mismatch $\Delta k_z L_{abs}$, where L_{abs} is the absorption length, at all measured peaks of the PDC rocking curves is about 0.1 radians, which is much smaller than 2π radians. As expected, the peak positions shift farther apart from the Bragg angle as the idler energy increases. This is because the k-vector of the idler also increases with the idler photon energy. These are clear indications that the rocking curves in Fig. 3.3 constitute conclusive evidence that we observe x-ray PDC signal.

3.1.4. Spectral measurements and discussion

Next we explore the dependencies of the signal count rates and the rocking curve peak positions on the photon energy of the idler and show that as predicted by my model described in Subsec 3.1.2, the dependencies are not monotonic in the energy range of 28-54 eV, which is far from any atomic resonances. For this purpose we measure rocking curves similar to those shown in Fig. 3.3 for photon energies of the signal in this range in steps of 1 eV. In Figs. 3.4 (a) and 3.4 (b) I present the measured count rates at the peaks of the rocking curves (power spectrum) and relative positions of the rocking curve peaks with respect to the angle of the elastic Bragg scattering as a function of the photon energy of the idler. In the measured power spectrum we see structures around 36 eV and 42 eV as predicted by the model from Subsec. 3.1.2. The existence of this non-monotonic dependence of the power spectrum on the idler photon energy, indicates that the underlying physical mechanism for the nonlinear interactions must include origin that is not from atomic interactions since the obtained spectral structures are far from any atomic resonances. According to the theory I provide in Subsec 3.1.2., it can be explained by including interactions with bulk plasmons.

While the experimentally observed structures of the power spectrum indicate clearly on the nonlinear interactions with the bulk plasmons, the detailed comparison with the theory requires the full simulation of the x-ray into UV PDC process since the count rate of the signal depends not just on the nonlinear coefficients but also on the refractive index and the absorption, which are also photon energy dependent. The simulation of the process is done by solving the coupled wave equations in the Heisenberg-Langevin model [16] as described in Subsec. 1.2. together with the model of nonlinearity provided above. The count rate is calculated by integration the solution

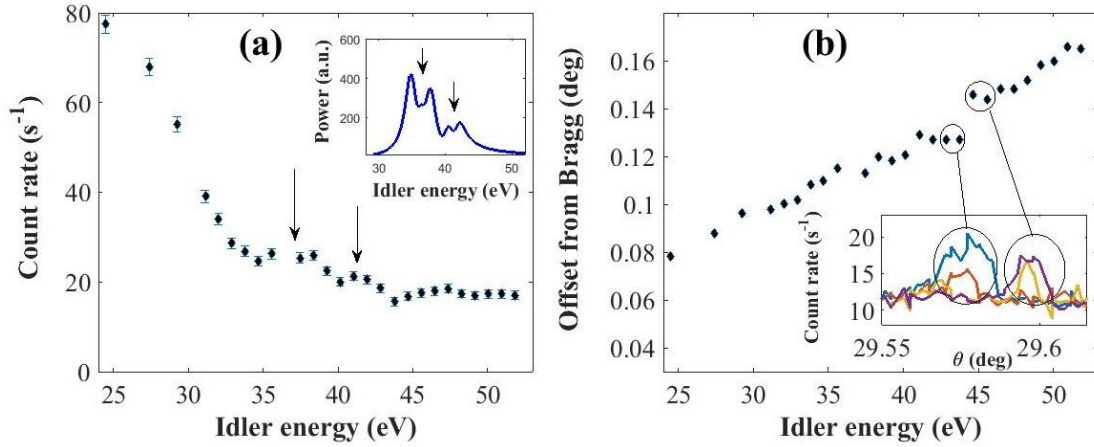


Figure 3.4 Experimental results showing the spectral dependencies on the idler photon energy of (a) the efficiency of the PDC and (b) the peak position of the signal beam. In (a) the arrows point to photon energies at which the theory that includes the interaction with plasmons, predicts peaks. The inset presents the simulation of the PDC process and the arrows point at energies that correspond to the position of the measured spectral peaks. In (b) the inset shows the rocking curves of the PDC at the photon energies near the sharp change in the peak position as a function of the idler photon energy.

for the signal over the photon energies and the solid angle of the experimental detection system. The results of the simulation are shown in the inset of the Fig. 3.4 (a) where the arrows point at the positions of the measured spectral features. It is important to note that most of the features from the calculated current density appear in the measured power spectrum. The measured features are wider than predicted by the simulation and some of the spectral features predicted by the theory are not resolved in the experiment due to the limited measurement resolution. The simulation also predicts a much higher enhancement of the x-ray PDC efficiency near ω_{NL} than the efficiency we observed in the experiment. This is probably because of losses that are associated with the energy transfer to bulk plasmons that I did not include in the simulation. The selection rules for the nonlinear interactions are also needed to take into account in order to improve the agreement between the experiment and the theory. Additionally, one may see that below the plasma frequency the theory and the experiment diverge dramatically. I

believe that in this spectral region the band structure plays the dominant role in forming the nonlinear mechanisms.

Another interesting spectral feature is found on the spectrum of the relative peak position. In Fig. 3.4 (b) there is a distinct sharp change in the curve at around 45 eV, which is also seen in the inset that shows the rocking curves of the signal at the corresponding points. Interestingly, the comparison with Fig. 3.4 (a) indicates that at the same photon energy there is a small dip in the power spectrum. This feature does not appear in the simulation and requires a separate study.

In order to conclude this Section, I provide a brief summary on this project. We have observed experimentally non-monotonic photon energy dependencies of PDC of x rays into UV far from any atomic resonances. These results cannot be explained by theories that consider only atomic or bond charge responses. I have proposed and described an explanation for the photon energies dependencies in the measured range by adding interactions with bulk plasmons to the classical model. While the main idea of strong photon energy dependencies near the nonlinear plasmon resonances is clearly shown in the experimental results, there are still some fine structures in the measured spectrum that call for a more comprehensive model of the nonlinearity of solids that includes multiple resonances and the effect of the crystal field.

The summary of this project is published as a Letter in Physical Review Letters [37].

3.2. Nonlinear optical response in metals

3.2.1. Introduction

Another fundamental collective electronic phenomenon is the Fermi surface in metals. The Fermi surface comprehensively describes such important properties of solids as electrical and thermal conductivity, magnetoresistance *etc.* [66]. Nowadays experimental studies of Fermi include such methods as Angle-Resolved photoemission spectroscopy - ARPES [40], in which the SR at UV frequencies is utilized to kick out the electrons from material and then analyze the photoelectric current with a detector

of electrons with momentum resolution. Despite the fact that this technique is well developed and provides amazing results, it requires suitable SR which already limits the application of the method and also rather expensive electron detectors. Another method one can study Fermi surface is analyzing the Compton scattering profile [43]. It requires complicated density-functional theory (DFT) calculations and again SR because the effects associated with Fermi surface are weak. The access to the Fermi surface can also be done via the oscillation of magnetic susceptibility (de Haas-van Alphen effect) or electrical resistivity (Shubnikov-de Haas effect) [67]. This approach requires high magnetic fields and vacuum. Magnetic fields in those experiments should be high enough so that the circumference of the cyclotron orbit would be smaller than a mean free path. Thus, the experiments usually performed at external high-field facilities. To be clear, I am not trying to diminish the significance of the mentioned methods. I am pointing out that the accessibility of the current tools in fermiology is not that high, which, in turn, slows down the progress. X ray into UV PDC can provide information about the Fermi surface. Despite the fact that I am describing the synchrotron experiments here, this is a proof-of-concept, and as we shall see in the next Section 3.3. the x ray into UV PDC experiments can be performed in the lab environment.

In this Section I present preliminary results of an experiment where the nonlinear optical response from a metal, namely, an Aluminum crystal, was observed. This is the first measurement of x ray into UV PDC from metals. I will discuss the spectra from the Aluminum crystal for two different reflections in the energy range where we expect to see the response from the Fermi surface.

Since the current experiment was conducted at the same GALAXIES beamline of the SOLEIL Synchrotron facility as the experiment described in previous Section 3.1. the experimental procedure was already well established and described in Subsec. 3.1.3.

3.2.2. Substantiation of the experiment

The main idea is that the nonlinear susceptibility $\chi^{(2)}(\vec{r})$ incorporates the linear susceptibility $\chi^{(1)}(\vec{r})$. The calculations of Lindhard functions [68] for free

electron gas show that the linear susceptibility has dependence of Fermi energy and momentum [69]. Thus we expect the contribution in the x-ray into UV PDC from the nonlinear optical response from the Fermi surface. In Fig. 3.5. the calculations of the linear susceptibility using Lindhard approach are shown. The following notations are used: $F(q) = -\text{Re } \chi(q, 0)$ is the static response function corresponding to zero energy transfer, $q = \frac{k}{k_F}$ is the normalized momentum to the Fermi k -vector, and

$\nu = \frac{\hbar\omega}{E_F}$ is the normalized energy to the Fermi energy.

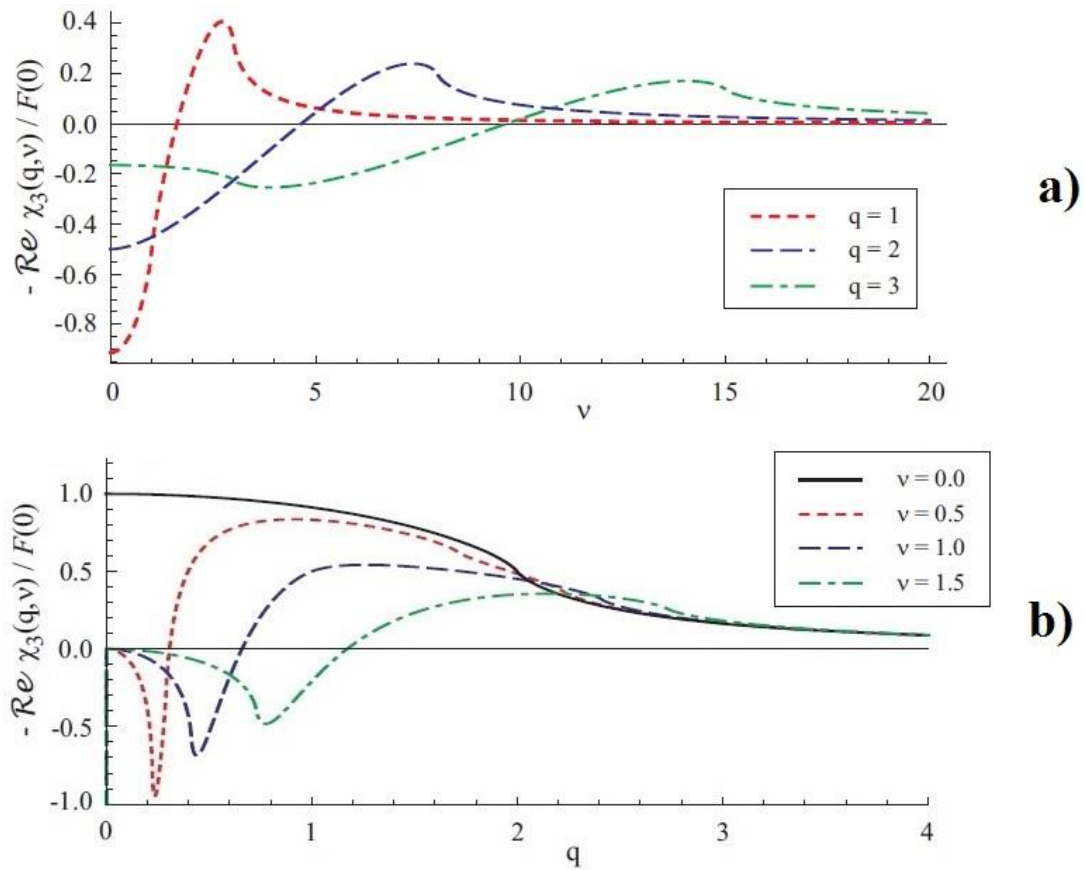


Figure 3.5 Energy (a) and momentum (b) dependence of the 3-dimensional Lindhard functions χ_3 . Both momenta and energies are expressed in terms of the

Fermi momentum k_F , and the Fermi energy $E_F = \frac{\hbar^2 k_F^2}{2m}$ [69].

Aluminum is a textbook example of a trivalent nearly-free-electron metal with electronic configuration $3s^23p^1$. The Fermi wave-vector in Aluminum crystal is $1.75 \times 10^8 \text{ cm}^{-1}$, the Fermi energy is 11.63 eV [66]. During the x-ray PDC process no momentum is transferred to an electron unlike in Compton process. However, since the reciprocal lattice vector is used to achieve the phase-matching conditions, momentum is transferred to the lattice. The corresponding energy transfer is very small comparing to the x-ray and UV energies (the characteristic energy of phonons is on the order of meV) so we neglect this energy transfer when we write the energy conservation law $\hbar\omega_p = \hbar\omega_s + \hbar\omega_i$.

The wave-vector corresponding to the momentum transfer to the Al(200) reciprocal lattice vector is $4.94 \times 10^7 \text{ cm}^{-1}$ and for Al(400) it is equal to $0.99 \times 10^8 \text{ cm}^{-1}$. In terms of the normalized momentum $q = \frac{k}{k_F}$ they are equal to 0.3 and 0.6 respectively. From the Fig. 3.4. (b) we can see, for example, that in the spectrum around the Fermi energy we expect to see contribution from the Fermi surface should be present in the measurement for Al(200) reflection whereas for Al(400) it should be absent. The examples of the rucking curves in Al(200) and Al(400) for idler energy of 19 eV are depicted in Fig. 3.6 (a) and Fig. 3.6 (b) respectively.

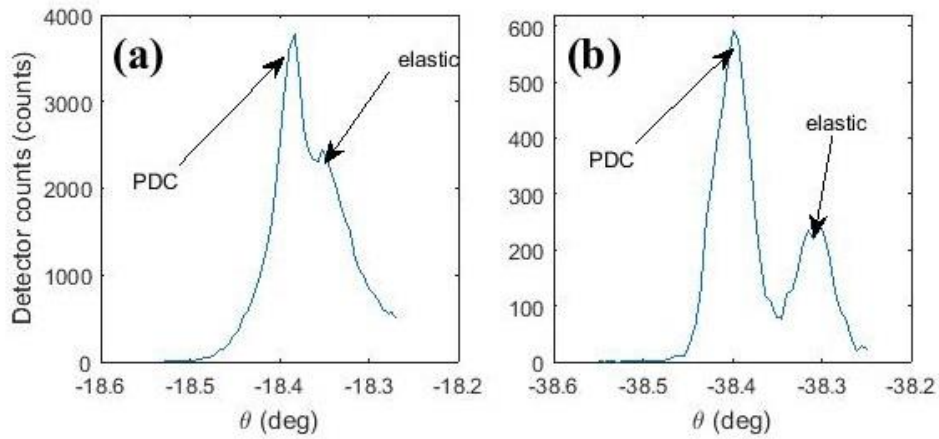


Figure 3.6 Examples of rocking curves from the aluminum crystal for the idler energy of 19 eV for two reciprocal lattice vectors corresponding to (a) Al(200) and (b) Al(400).

3.2.3. Aluminum spectra and discussion

By following the same experimental procedure described in Subsec 3.1.3. we have measured the rocking curves of the x-ray into UV PDC effect in Aluminum crystal for the idler energies in the range of 5-35 eV for Al(200) reflection and 10-35 eV for Al(400) reflection. The collected spectrum is depicted in Fig. 3.7.

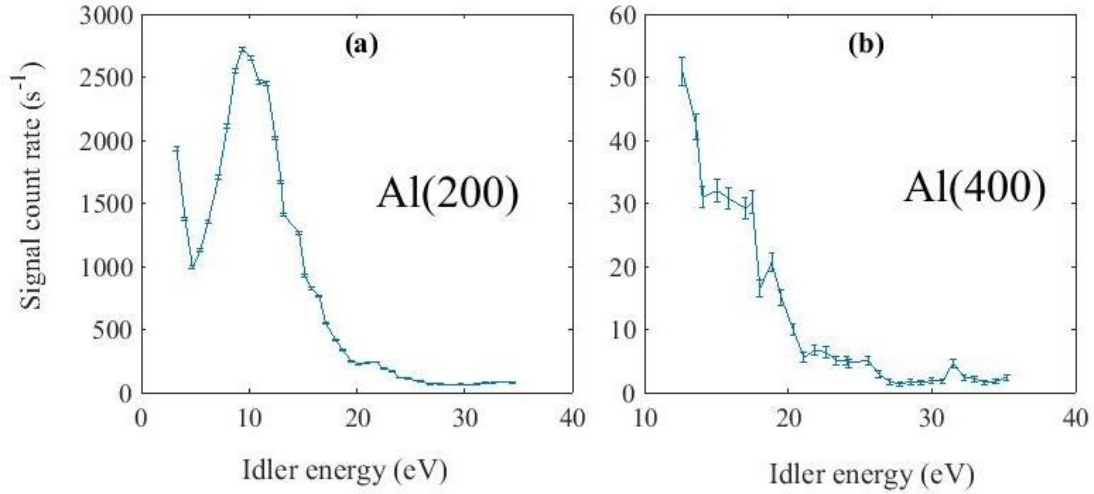


Figure 3.7 Spectral dependence of the x-ray into UV PDC process for Al(200) (a) and Al(400) (b) reciprocal lattice vectors respectively.

In Fig. 3.7 (a) we see a pronounced peak around 10 eV which might indicate the response from the Fermi level. However, the contribution from the plasma oscillation described in Section 3.1. are not to be neglected. The calculation of the nonlinear resonances $\hbar\omega_{NL}$ gives us value around 15 eV. During this calculations I put the resonance energy $\hbar\omega_0$ to zero, which for metallic samples with nearly-free conduction electrons is justified. Thus, only the bulk plasmons contribution is considered. In other words, the high peak with the center at 10 eV and width of about 7 eV might be a combination of contributions into the nonlinear optical response from the Fermi surface and bulk plasmons. Separation of them is indeed an open question. For the Al(400) (Fig. 3.7 (b)) the measurement of the signal in the energy range of Fermi energy was not possible at the moment due to the strong background noise that

swamps the signal. We also see a feature (a step) around 21-22 eV that might correspond to the response from twice the Fermi energy on both spectra. However, it is hard to make conclusions on their nature considering the lack of the calculations of the nonlinearity that would include Lindhard approach. I note, that a feature that possibly corresponds to the nonlinear bulk plasmon resonance $\hbar\omega_{NL}$ around 15 eV is more pronounced in spectrum for Al(400) reflection.

In conclusion, I present the measurements of x-ray into UV PDC on metals, namely Aluminum, for the first time. The measurements are done in a wide energy range, the spectrum collected for two reciprocal lattice vectors. Despite the fact that the interpretation of the results is rather speculative, I believe that this is a good starting point to open a discussion about contribution of the Fermi surface into the nonlinear optical response. I believe this will open an exciting new field of application of x-ray into UV PDC process. For the design of further experiments I think the reciprocal lattice

vector corresponding to the $q = \frac{k}{k_F}$ equals to 1 and 2 should be considered in order to track the same energy spectral dependence as is shown in Fig. 3.5 (a) rather than observing the momentum spectrum. For x-ray into UV PDC experiments it is more justified.

3.3. High energy-resolution measurements of x-ray into ultraviolet parametric down-conversion with an x-ray tube source

3.3.1. Introduction

At this point one may understand that x-ray into UV PDC has a great potential becoming a powerful tool for the studies of electronic properties in crystals. Indeed, several experiments have advanced these efforts [28, 31, 33, 35-38]. However, a practical application requires energy resolution of a few eV or less. Thus far we have

discussed only synchrotron experiments where this requirement has been achieved. It is desirable, of course, that x-ray into UV PDC measurements could be done using laboratory equipment. Such possibility would broaden dramatically the application and further development of the nonlinear x-ray spectroscopy.

However, it is not obvious that the measurements of x-ray into UV PDC can be done with laboratory sources for several reasons; first, the low efficiency leads to very low count rates and to the requirement of a very careful design of the experiment to avoid signal loss. This is true for synchrotron experiments but it is much more severe with laboratory sources. The second major reason is the strong divergence of the beam in the direction normal to the scattering plane of the sample in laboratory systems. This divergence is a consequence of the trade of between flux and divergence. In practice the divergence angle is a few mrad versus tens of μrad at synchrotron facilities. Consequently, in contrast to synchrotron experiments it is not possible to achieve high resolution with laboratory sources with analyzer crystal operating in the plane normal to the scattering plane of the sample. Thus the angle of the analyzer, the source angle, and the detector arm angle are coupled. The third reason is the short distances between the sample and the analyzer and between the analyzer and the detector as imposed by the enclosure of the laboratory sources, which introduces a challenge in separating the signal from the background. By this moment there was only one report about experimental demonstration of x-ray into UV PDC with an x-ray tube source, the energy resolution was limited by the energy resolution of the detector, which is larger than 125 eV [30].

In this Section I will describe experiments demonstrating the ability to perform high-energy resolution measurements of x-ray into UV PDC with with laboratory x-ray systems. I would like to note that this project is a joint project was done with another member of our group Shiran Levi. I will present the results of measurements of x-ray into UV PDC on Diamond and Lithium Fluoride crystals.

All the phase-matching considerations from previous sections such as energy conservation $\hbar\omega_p = \hbar\omega_s + \hbar\omega_i$ and momentum conservation $\vec{k}_p + \vec{G} = \vec{k}_s + \vec{k}_i$ are applied. The phase-matching scheme is depicted in Fig. 3.8 (a). Here θ_p , θ_s , and θ_i is the angle with respect to the atomic planes of the pump, signal, and idler respectively. k_B is the k-vector that satisfies the Bragg condition. Following the same idea that the

generated photons are correlated and that the rate of generated signal photons depends on both x-ray and UV properties of material, we measure only x-ray photon to retrieve the information on the UV interactions.

3.3.2. Experimental setup and noise level evaluation

We used the Rigaku Smartlab 9kW x-ray diffractometer (XRD) with a rotating anode. The schematic of the experimental setup is depicted in Fig. 3.8 (b). The pump beam is a fluorescence line Cu $K\alpha 1$ of a cooper anode (8.047 eV) further collimated and monochromatized in order to reduce the parasitic radiation. The incident optics for this purpose includes a parabolic multilayer mirror; the source of x rays is placed in the focus of this mirror and results in a well-collimated beam. Then a parallel beam slit picks only a central part of the beam in order to make even more collimated. Then the beam goes through a Germanium 2-bounce single-cut crystal monochromator where it reflects by Bragg mechanism from two parallel surfaces with Ge(220) orientation which makes a beam monochromatic. The receiving optics, in turn, includes an adjustable slit to limit the angular acceptance, 2-bounce Germanium analyzer Ge(220)

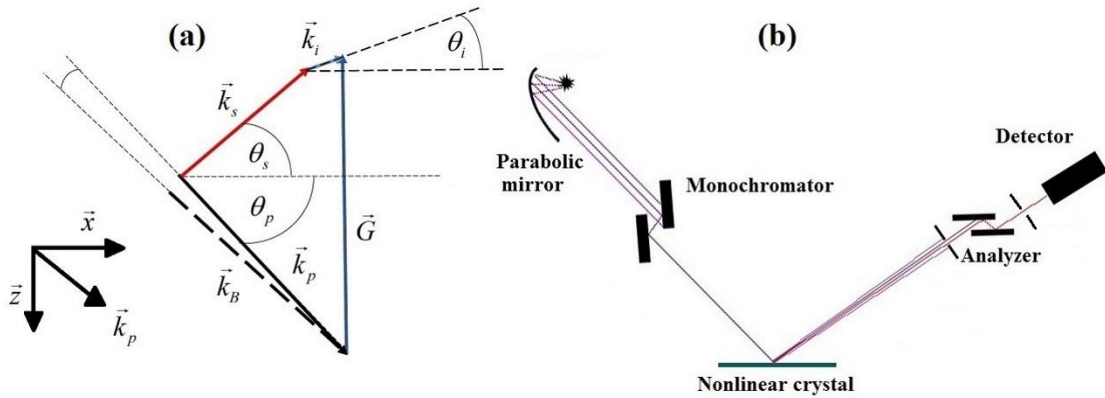


Figure 3.8 (a) Phase-matching scheme. The indices k_p , k_s , and k_i are the k-vectors of the pump, signal, and idler respectively. G is the reciprocal lattice vector. k_B is the k-vector of the Bragg diffraction. (b) Experimental setup.

In the lab we have two 2-bounce single-cut analyzers, Ge(220) and Ge(400). The reason of choosing Ge(220) is that it provides us acceptable angular resolution of about 0.01 degrees and the crystal structure factor of the Ge(220) reflecting plane is larger than that of Ge(400):181.8 for Ge(220) versus 155.1 for Ge(400). This results in the higher intensity at the output. The spot size at the sample is about $2\text{mm} \times 1\text{mm}$, the incident flux is about 4×10^8 c.p.s., the angular divergence of the system is about 0.04 deg, and the beam is not polarized. In order to observe weak effects such as x-ray PDC, we use a commercially available Silicon-Drift Detector (SDD) with very low dark noise (1 count per 1000 sec).

We calibrate the analyzer with Cu $K\alpha 1$ and Cu $K\alpha 2$ lines from the anode, and also with bremsstrahlung since it contains a very broad range of photon energies. We select a certain wavelength by the input monochromator, find the Bragg reflection from a reference Si(400) crystal and then find the corresponding angle of the analyzer. We estimate the energy resolution of the analyzer to be about 3 eV with respect to the FWHM of the copper $K\alpha 1$ line.

At this point I would like to discuss the differences between our experimental setup and the one that was used by Danino and Freund in the very first observation of x-ray into UV PDC using an x-ray tube [30]. First, we have the parabolic multilayer mirror that provides a well collimated beam resulting in a higher count rate at the sample surface. Second, the adjustable analyzer with energy resolution of few eV that allows to perform a spectroscopy measurements with high energy resolution. I note that at the moment of Danino and Freund experiment the single-cut crystal analyzers (and monochromators) were not commercially available.

Next, I will discuss the possible sources of noise in the system. The main noise comes from the tail of the Bragg scattering. The efficiency of this elastic process is many orders of magnitude higher than the efficiency of x-ray into UV PDC. Indeed, as we will see further, even after the analyzer crystal we find non-negligible background from the Bragg tail. Fortunately, the Bragg reflection is narrower than the rocking curve of x-ray PDC and thus we can separate them spatially by scanning over the angle of the source. The next potential noise is Compton scattering. Since the energy of the pump radiation is much smaller than electron rest energy (511 keV), Klein-Nisina formula for

Compton cross-section is reduced to Thomson cross-section. Thus the differential cross section formula for unpolarized light is [52]

$$\frac{d\sigma_{Th}}{d\Omega} = \frac{r_e^2}{2} (1 + \cos^2 \theta) , \quad (3.3.1)$$

where θ is the scattering angle, Ω is the solid angle. The power radiated into the solid angle will be then:

$$I_{compt} = n_e L I_{in} \int_{\Omega} d\sigma_{Th} , \quad (3.3.2)$$

where n_e is the electron number density, I_{in} is the incident radiation and L is the absorption length. The calculation for diamond crystal (4 mm × 4 mm × 0.8 mm), Cu K α radiation, incident power of 4×10^8 photons/sec, the slit size 0.2 mm, and the distance between the crystal and the slit of 17 cm gives us count rate of the Compton scattering about 1.6 photons/sec before the analyzer. For LiF crystal this value is about 0.5 photons/sec. Moreover, the Compton shift in experiment with diamond was about 95 eV from the elastic and 150 eV in case of LiF experiment. Since those energies are far from the idler energies considered in the experiment, the energy resolution of the analyzer crystal is sufficient to filter out the Compton scattering very efficiently. Another possible source for noise is x-ray Raman scattering, but this effect is weak far from resonances in comparison with Compton scattering [43, 70].

Finally, consider the noise coming from fluorescence. The fluorescence is coming mostly from different parts of the experimental setup since the deepest absorption edges of the samples used in the current experiments are at low energies (280 eV for Diamond and 692 eV for Fluorine). Since the calculation of the fluorescence is a rather non-trivial task in the case when we do not know exactly the source of it, I present a direct measurement depicted in Fig. 3.9. This measurement was done for the LiF crystal, for the Diamond the situation is similar. The high peak corresponds to the Bragg tail which we have discussed before. We can see that the analyzer reduces fluorescence by an order of magnitude to a negligible level. Nevertheless the lines are pronounced even after the analyzer. This is because the fluorescence does not have an angular dependence and being generated at different

places along the beam propagation so there are always some wave vectors that will reach the Bragg condition of the analyzer crystal.

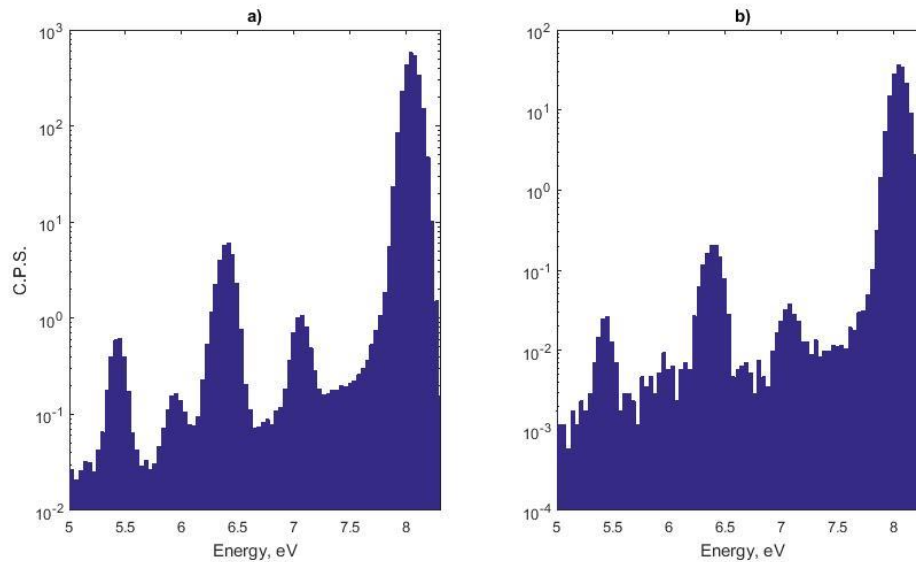


Figure 3.9 Fluorescence measurement in LiF a) without the analyzer and b) with the analyzer.

3.3.3. Experimental procedure and results

Now I will describe an experimental procedure. We begin by finding the Bragg reflection and measuring the rocking curve with the analyzer tuned to the $\text{Cu } K\alpha 1$ line. Next, we move the source and the detector to the PDC phase matching angles. The analyzer is set to the photon energy of the signal photon. We use slits before and after the analyzer to select a narrow angle range and to filter out residual elastic scattering. We first scan over the angle of the source with respect to the crystal. Then we optimize the signal and signal-to-noise-ratio by scanning over the detector arm and the analyzer angle. For the phase-matching we use the (220) reflection for the measurements in diamond and the (400) reflection in the measurements in LiF.

Fig. 3.10 shows the signal count rate as a function of the deviation of the pump angle from the phase matching angle, which we denote as Δq_p . These measurements are done by scanning the angle of the source where all other angles are fixed. The solid

lines are the theoretical calculations where we use the free-electron nonlinearity described in Subsec. 1.2. without including resonance effects together with the coupled wave equations for the signal and idler operators in the slowly varying envelope approximation as described in Subsec. 1.3. Fig. 3.10 (a) depicts Dq_p scans for the diamond crystal. The idler energy is 30 eV, and the phase matching angle is 2 mrad from the Bragg angle. It is clear that the PDC peak is shifted from the exact phase-matching angle. The same shift is shown in the theoretical calculations as well. The two sharp peaks at -0.11 deg and at zero are due to the residual Bragg diffraction, the left peak matches the offset from the Bragg angle so it originates from the Bragg tail. The peak at zero occurs when the source and the detector are in mirror-like position. Since the analyzer works in the scattering plane at some angles the situation where the reflected beam reaches the detector without hitting the analyzer crystal might occur. In Figs. 3.10 (b) and 2 (c) the measurements for the LiF crystal for the two possible solutions of the phase-matching equation $\vec{k}_p + \vec{G} = \vec{k}_s + \vec{k}_i$ are shown. The detector angles 0.3184 degrees and -0.2185 degrees in accord with Bragg correspondingly. The idler energy is 40 eV and the offset from the Bragg angle is 5 mrad. We find that the calculated count rates are smaller by a factor of about 5 from the measured count rates and that the measured rocking curves are broader than the theoretical prediction.

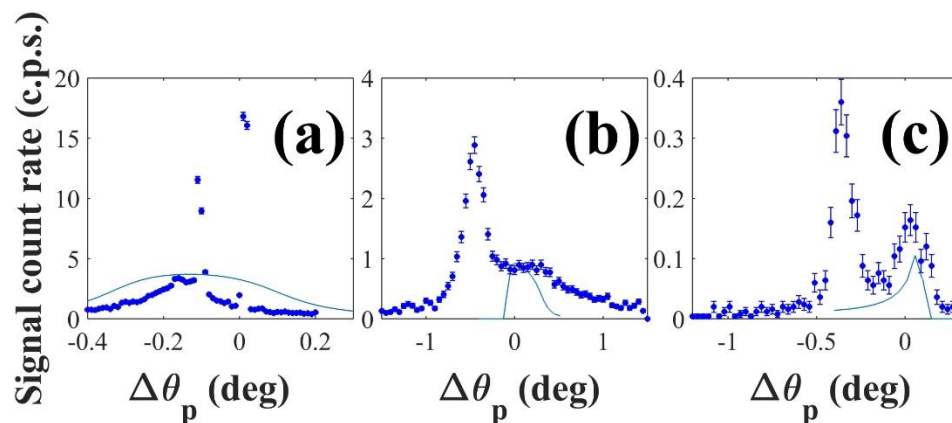


Figure 3.10 Signal count rate as a function of the deviation from phase matching for (a) diamond and (b) and (c) LiF. (b) and (c) correspond to two solutions of the phase-matching equation, with a larger and a smaller angle in accord with the Bragg angle, respectively. The idler energies are 30 and 40 eV

for diamond and LiF measurements respectively. The zero on the abscissa corresponds to the phase-matching condition. Dots with error bars are the experimental measurements; the solid lines are theoretical simulations. The PDC curves are the board curves. The strong sharp peaks are due to the Bragg reflection. The theoretical calculations for LiF are multiplied by a factor of 5.

The discrepancies in the widths can be explained by the mosaic spread of the LiF crystal. To reconcile between the theoretical and measured efficiencies a quantum model, which consider local field correction for the nonlinearity, is most likely required. I emphasize that both the theoretical calculations and the experimental measurements show the shift of the maximum of the PDC effect from the exact phase-matching angle. The shift depends on the phase-matching equation solution and on the offset from Bragg condition. Interestingly, the measured efficiencies of the PDC for the two solutions of the phase-matching equation (shown in Fig. 3.10 (b) and in Fig. 3.10 (c)) are not equal in agreement with the theoretical calculations. The strong peaks on the left of the PDC curves also originate from the Bragg tail. The position matches the offset from the Bragg angle considering the mosaic spread of the crystal and rather broad (about 0.1 deg) rocking curve of the Bragg reflection.

To understand the shift in the curve with respect to the phase matching we recall that a large number of vacuum modes contribute to the PDC effect and that there is a one-to-one correspondence between the photon energies and the angles imposed by the phase matching condition. Since the detector has a finite aperture, modes at many photon energies and angles are collected and modes with $\Delta k_z \neq 0$ also contribute to the count rate. The measured count rate is the sum of all the possible modes that are limited by the acceptance angle of the detector, by the bandwidth of the analyzer, and by the boundary conditions. In addition, since the nonlinearity increases as the idler photon energy decreases, the contributions of the lower photon energy modes are larger. This leads to the asymmetric line shape and to a shift in the rocking curve. The difference between the efficiencies at the different phase matching solutions is because the angles of the idler photon with regard to the crystal surface are different for the two solutions.

Next, we explore the spectral structure of the scattered beam. Fig. 3.11 (a) shows the analyzer scans at idler photon energies of 30 eV (empty circles), 40 eV (green

circles), and 50 eV (black triangles). The size of the slit before the analyzer is 0.1 mm. Apart from the sharp and narrow elastic peak that corresponds to the residual elastic scattering, we see a broad peak at each of the curves. The energy of this peak corresponds not to the selected idler photon energy but to the binding energy of 2p electrons in diamond at 11.3 eV [71]. At this energy the PDC effect is much stronger because of the resonant enhancement of the nonlinear susceptibility due to the vicinity to the absorption edge [35]. The curves of the analyzer scans are broad because numerous vacuum fluctuation modes contribute to the count rate. The heights of curves decrease as the idler energies increase as expected. We note that the elastic peak is shifted from its position when the angles of the source and the detector satisfy the Bragg condition. This is because the analyzer crystal and the sample have the same scattering planes. Fig. 3.11 (b) shows the analyzer scan for the LiF crystal at the phase-matching. The main peak is around 5 eV and corresponds to the 2s electrons of the Li atoms [71]. Inset (ii) reveals a bump near 17 eV, which corresponds to the 2p electrons of the Fluorine atoms [71]. Finally, inset (iii) shows a hump that corresponds to the signal for the chosen idler energy at 40 eV.

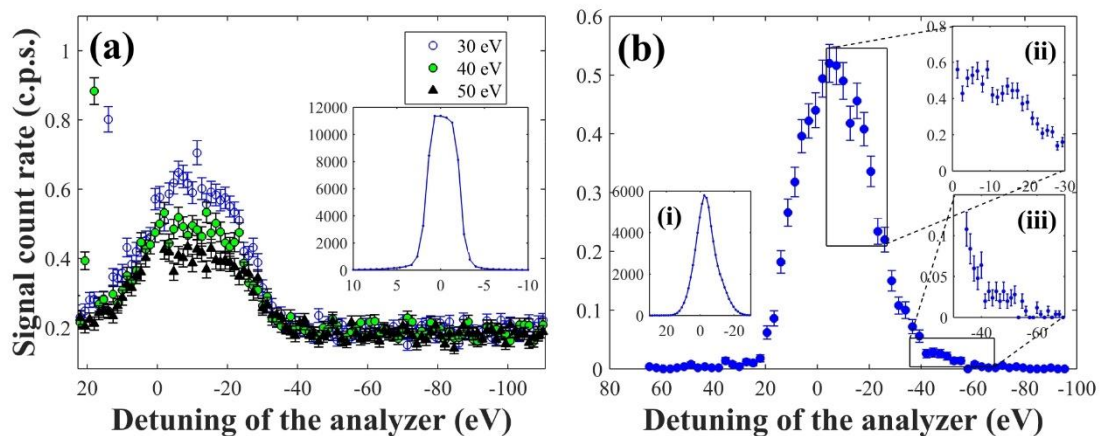


Figure 3.11 Signal count rate versus the analyzer detuning from the pump energy for different phase-matching conditions of (a) diamond and (b) LiF. The zero on the abscissa axis is the pump energy. In (a) the legend represents the idler energy. The inset shows the scan where the diamond is at the Bragg condition. (b) Analyzer scan at phase matching for idler energy of 40 eV and offset from the Bragg angle of 5 mrad. The inset (i) shows the scan at the Bragg

condition. Insets (ii) and inset (iii) show features of the spectrum, which are discussed in the text.

3.3.4. Spectrum of LiF and discussion

Another interesting phenomenon occurs when the idler energy is chosen to be close to absorption edges [35] as is shown in Fig. 3.12, which describes the spectral dependence of the PDC in the LiF crystal. Each of the points in this figure represents the peak of the rocking curve at the idler energy of the horizontal axis. We clearly see a strong peak near the L_I absorption edge (2s level) of the fluorine atoms at 37 eV. The peak is shifted to the higher energies in agreement with previous observations [72]. The authors of Ref. 35 suggest that the resonant behavior of the PDC occurs when the atomic structure factor f_l becomes negative. In the current case the tabulated values of f_l for fluorine are positive [73]. However, it should be noted that those tabulate values are not accurate in the UV range. In particular, they do not show any resonance in the spectral dependence of f_2 of the fluorine near 37 eV in contrast to previous experimental and theoretical reports [72, 74, and 75]. Therefore the comparison with theory requires more accurate theoretical calculations for solids since they are different than the structure factors calculated for atoms.

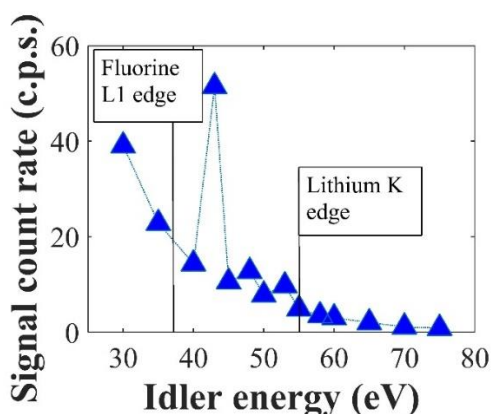


Figure 3.12 Spectral dependence of the efficiency of PDC process in LiF. The vertical black solid lines correspond to the L_I edge of the neutral fluorine atom and the K edge of neutral lithium atom.

To summarize this Section, I described the principal feasibility of performing x-ray into UV PDC experiments with energy resolution of few eV using a standard laboratory diffractometer with minor modifications. We can make several conclusions from the presented experimental data. The results suggest that classical free-electron model of nonlinearity is adequate for the description of x-ray into UV process far from resonances in Diamond. For LiF, however, the predicted efficiency is about five times weaker than the measured efficiency and the model does not show any resonance near 43 eV in contrast to the experiments. Hence a different model for nonlinearity should be considered. We showed that the efficiency of the effect varies rapidly near the L_1 -edge of fluorine and the K -edge of the lithium and conclude that it is therefore atomic selective. The relatively simple setup of the experiments we described, and the availability of commercial detectors with very low dark count noise open a possibility for broader studies on electronic properties of materials using x-rays into UV PDC with low brightness systems. The observation of the effect with low flux advances the possibility for applications in spectroscopy of samples with very low radiation damage threshold such as biological samples.

The summary of this project was published in 2017 in a peer review journal Applied Physics Letters [39].

Chapter 4

Conclusions and outlook

4.1. Summary of my works

Summarizing the results of my PhD studies, I can divide it into two main parts that corresponds to two different regimes of the x-ray PDC process. They are detailed in Chapter 2 and 3 respectively.

The project described in Chap. 2 describes the method of generating nearly collinear x-ray photon pairs using the effect of x-ray PDC. In this Chapter I described how to overcome the main challenge that inhibits development of experiments with paired x-ray photons. In order to obtain reasonable count rate one cannot simply increase the input flux for it saturates the detectors due to strong linear processes such as Bragg diffraction and Compton scattering. We utilized the polarization properties of both linear (described by the Thomson differential cross-section) and nonlinear (described by the nonlinear current density) processes. The analysis shows that by choosing scattering angle of 90 degrees, the linear processes are highly suppressed and the photons generated via x-ray PDC are visible in the coincidence spectrum even without energy discrimination filter unlike all previous reports. I would like to note that this work has made already a certain impact on the field of quantum x-ray optics. A few experiments in which I have participated and contributed have been performed based on the described experimental setup: quantum ghost imaging [21] in which we have shown the first application of the correlated x-ray photon pairs and another experiment in which we have shown single-photon nature of x-ray Bragg diffraction [23]. Another

experiment using this setup was performed in which the authors show quantum properties of the generated photons by showing sub-Poissonian distribution of the generated pairs [22]. Before that quantum nature of the generated photons has not been proven strictly.

In the second part of the thesis described in Chap. 3 I study another regime of x-ray PDC, namely x-ray into UV PDC with respect to its application in novel nonlinear x-ray spectroscopy. In Sec. 3.1. I provide a theoretical and experimental study on x-ray into UV PDC spectral properties far from atomic resonances. I show the existence of the spectral feature in the energy region 30 - 54 eV that cannot be explained by the models that do not include collective phenomenon. I provide a classical model of nonlinearity that takes into account interactions with bulk plasmons, that describes the observed spectrum in this region.

In Sec. 3.2. I describe the first observation of x-ray into UV PDC in metals. I provide spectra taken from an Aluminum crystal for two reciprocal lattice vectors and discuss the possibility of the contribution of another fundamental collective phenomenon – Fermi surface – into the nonlinear optical response. Due to the lack of a comprehensive model of nonlinearity supporting x-ray into UV PDC, the interpretation of the results is rather speculative. However, there are spectral feature around 21 eV that is present on both spectra that corresponds to the twice the Fermi energy. This might indicate the nonlinear optical response from the Fermi surface and opens a possibility to extend the studies on the Fermi surface using the effect of x-ray into UV PDC.

Sec. 3.3. describes experiments in the lab environment in collaboration with another member of our group Shiran Levi. I provide the schematic of the experimental setup and procedure of observing x-ray into UV PDC using a conventional x-ray diffractometer with an x-ray tube source. The x-ray PDC rocking on diamond and a spectrum from LiF is provided. The dependence on the absorption edge L_I in the spectrum of LiF is clear. This project increases the availability of the method significantly. While the previous experiments was conducted using SR, they are proof-of-principle experiments, this work shows that it is possible to bring the nonlinear x-ray spectroscopy based on x-ray PDC in a laboratory rather than being performed at external facilities such as synchrotrons.

4.2. Further studies

In the discussion below I provide details and ideas of possible directions for future research based upon the studies presented in this dissertation.

Within the frame of x-ray into x-ray PDC, I believe that the developed geometry of an experimental setup will be further used in x-ray quantum optics experiments using paired x-ray photons. As an obvious example, one may think of extending quantum optics experiments into x-ray regime such as Hong-Ou-Mandel effect [50] and the Bell inequality [51]. Ghost imaging techniques based on this effects may also find application due to very high SNR which allows to image an object with a very small number of photons. This is useful, for instance, in case of objects with low radiation damage threshold such as biological samples.

Further way of the nonlinear x-ray spectroscopy technique based on x-ray into UV PDC can be divided into the following directions: theoretical study, synchrotron experiments, and further development of the experiments using an x-ray tube source. Theoretical challenges in this field are huge and the lack of a comprehensive model of nonlinearity slows down the development and broad application of the technique. The model should include both local and collective phenomena, free-electron and band structure contribution into the nonlinear optical response. The selection rules of band transitions participating in the nonlinear interactions with bulk plasmons are also to be clarified. Nonlinear spectroscopy experiments performed at synchrotron have a nature of proof-of-principles experiments and thus can develop the technique quicker. For example, an experiment for the further research on nonlinear interactions with bulk plasmons, one can collect the spectrum for different reciprocal lattice vectors to clarify the band transitions participating in the interactions. The different crystallographic directions in this case will reveal the contribution of plasmon dispersion in the crystal. In metals, it seems to be possible to continue developing the technique to study the Fermi surface. Aluminum seems to be a perfect candidate for the first steps in this direction since its electronic structure is well known and last but not least commercially available Aluminum single crystals are of good quality and relatively cheap. This is important since during a synchrotron experiment, strong SR damages the polished surface of an Aluminum crystal, which at a certain point affects the measurements. Another very interesting direction of studies using x-ray into UV PDC is to study phase

transitions. Since x-ray into UV PDC provides both structural information and probes the electron properties of materials in a single measurement, the effect seems to have a great potential to become a powerful tool in those studies. For example, metal-insulator transition in VO₂ can be performed to shed light on the question whether the system insulating because of electronic correlations or due to an opening of the gap by the Peierls mechanism. As for the lab studies, I can propose several ways of improving the setup: Using 2D detector instead of single pixel detector is extremely convenient. It removes the necessity of alignment of the detector and also removes the slit after the analyzer. All that can be done in the post analysis of the images from the 2D detector. The XRD system in our lab in principle allows to decouple the analyzer and the detector from the scattering plane. In this case using the 2D detector together with the channel-cut analyzer crystal will provide a scattering angle distribution of the x-ray PDC signal for each point of the rocking curve. Such 3D array is relatively simple to analyze and these data can be used to detail the propagation aspects of x-ray into UV PDC.

Bibliography

- [1] P. Emma *et al.*, “*First lasing and operation of an ångstrom-wavelength free-electron laser*”, *Nat. Photonics* **4**, 641 (2010).
- [2] H. Tanaka *et al.*, “*A compact X-ray free-electron laser emitting in the sub- ångström region*”, *Nat. Photonics* **6**, 540 (2012).
- [3] A. Altarelli, “*The European X-ray free-electron laser facility in Hamburg*”, *Nucl. Instrum. Methods Phys. Res. B* **269**, 2845 (2011).
- [4] K. Tamasaku *et al.*, “*X-ray two-photon absorption competing against single and sequential multiphoton processes*”, *Nat. Photonics* **8**, 313 (2014).
- [5] T. E. Glover *et al.*, “*X-Ray and Optical Wave Mixing*”, *Nature* **488**, 603 (2012).
- [6] S. Schwartz *et al.*, “*X-Ray Second Harmonic Generation*”, *Phys. Rev. Lett.* **112**, 163901 (2014).
- [7] R. K. Lam *et al.*, “*Soft X-Ray Second Harmonic Generation as an Interfacial Probe*”, *Phys. Rev. Lett.* **120**, 023901 (2018).
- [8] E. Shwartz and S. Shwartz, “*Difference-Frequency Generation of Optical Radiation from Two-Color X-Ray Pulses*”, *Opt. Express* **23**, 7471 (2015).
- [9] D. Bouwmeester, A. Ekert, and A. Zeilinger, *The Physics of Quantum Information: Quantum Cryptography, Quantum Teleportation, and Quantum Computation* (Springer, New York, 2000).
- [10] I. Freund and B.F. Levine, “*Parametric conversion of X rays*”, *Phys. Rev. Lett.* **23**, 854 (1969).
- [11] I. Freund, “*Nonlinear diffraction*”, *Phys. Rev. Lett.* **21**, 1404 (1968).
- [12] P. M. Eisenberger and S. L. McCall, “*X-ray parametric conversion*”, *Phys. Rev. Lett.* **26**, 684 (1971).
- [13] Y. Yoda, T. Suzuki, X.-W. Zhang, K. Hirano and S. Kikuta, “*X-ray parametric scattering by a diamond crystal*”, *J. Synchrotron Radiat.* **5**, 980 (1998).

- [14] B. Adams, *Nonlinear Optics, Quantum Optics, and Ultrafast Phenomena with X-Rays* (Kluwer Academic Publisher, Boston, 2008).
- [15] S. Shwartz and S. E. Harris, “*Polarization Entangled photons at X-Ray Energies*”, Phys. Rev. Lett. **106**, 080501 (2011).
- [16] S. Shwartz, *et al.*, “*X-ray parametric down-conversion in the Langevin regime*”, Phys. Rev. Lett., **109**, 013602 (2012).
- [17] R.L. Byer and S.E. Harris, “*Power and Bandwidth of Spontaneous Parametric Emission*”, Phys. Rev. **168.**, 1064 (1968).
- [18] D.N. Klyshko, “*Coherent photon decay in a nonlinear medium*”, JETP Letters **6**, 23 (1967).
- [19] D.A. Kleinman, “*Theory of optical parametric noise*”, Phys. Rev. Lett., **174**, 1027 (1968).
- [20] D. Borodin, A. Schori, F. Zontone, and S. Shwartz, “*X-ray photon pairs with highly suppressed background*”, Phys. Rev. A **94**, 013843 (2016).
- [21] A. Schori, D. Borodin, K. Tamasaku, and S. Shwartz, “*Ghost imaging with paired x-ray photons*”, Phys. Rev. A **97**, 063804 (2018).
- [22] S. Sofer, E. Strizhevsky, A. Schori, K. Tamasaku, and S. Shwartz, “*Quantum illumination with x-rays*”, Submitted
- [23] E. Strizhevsky, D. Borodin, and S. Shwartz, In preparation
- [24] I. Freund, “*Nonlinear X-ray diffraction. Determination of valence electron charge distributions*”, Chem. Phys. Lett. **12**, 583 (1972).
- [25] I. Freund and B. F. Levine, “*Optically modulated X-ray diffraction*”, Phys. Rev. Lett. **25**, 1241 (1970).
- [26] P. M. Eisenberger and S. L. McCall, “*Mixing of X-ray and Optical Photons*”, Phys. Rev. A **3**, 1145 (1971).
- [27] T. E. Glover, D. M. Fritz, M. Cammarata, T. K. Allison, S. Coh, J. M. Feldkamp, H. Lemke, D. Zhu, Y. Feng, R. N. Coffee, M. Fuchs, S. Ghimire, J. Chen, S. Shwartz, D. A. Reis, S. E. Harris, and J. B. Hastings, “*X-ray and optical wave mixing*”, Nature **488**, 603 (2012).

- [28] A. Schori, C. Bömer, D. Borodin, S. P. Collins, B. Detlefs, M. Moretti Sala, S. Yudovich, and S. Shwartz, "*Parametric Down-Conversion of X Rays into the Optical Regime*", Phys. Rev. Lett. **119**, 253902 (2017).
- [29] I. Freund, "*Nonlinear X-ray diffraction. Determination of valence electron charge distributions*", Chem. Phys. Lett. **12**, 583 (1972).
- [30] H. Danino, and I. Freund, "*Parametric Down Conversion of X Rays into the Extreme Ultraviolet*", Phys. Rev. Lett. **46**.17, 1127 (1981).
- [31] K. Tamasaku & T. Ishikawa, "*Interference between Compton scattering and X-ray parametric down-conversion*", Phys. Rev. Lett. **98**, 244801 (2007).
- [32] U. Fano, "*Effects of Configuration Interaction on Intensities and Phase Shifts*", Phys. Rev. **124**, 1866 (1961).
- [33] K. Tamasaku, K. Sawada & T. Ishikawa, "*Determining X-Ray Nonlinear Susceptibility of Diamond by the Optical Fano Effect*", Phys. Rev. Lett. **103**, 254801 (2009).
- [34] I. Freund and B. F. Levine, "*Resonant Dispersion of the Nonlinear Atomic Scattering Factor*" Opt. Commun. **3**, 101 (1971).
- [35] B. Barbiellini, Y. Joly & K. Tamasaku, "*Explaining the x-ray nonlinear susceptibility of diamond and silicon near absorption edges*", Phys. Rev. B **92**, 155119 (2015).
- [36] K. Tamasaku, K. Sawada, E. Nishibori & T. Ishikawa, "*Visualizing the local optical response to extreme-ultraviolet radiation with a resolution of $\lambda/380$* ", Nature Physics **7**, 705 (2011).
- [37] D. Borodin, A. Schori, J.-P. Rueff, J.M. Ablett, and S. Shwartz, "*Evidence for Collective Nonlinear Interactions in X Ray into Ultraviolet Parametric Down-Conversion*", Phys. Rev. Lett. **122**, 023902 (2019).
- [38] D. Borodin, E. Strizhevsky, J.-P. Rueff, J.M. Ablett, and S. Shwartz, In preparation
- [39] D. Borodin, S. Levy, and S. Shwartz, "*High energy-resolution measurements of x-ray into ultraviolet parametric down-conversion with an x-ray tube source*", Appl. Phys. Lett. **110**, 131101 (2017).

- [40] A. A. Kordyuk, “*ARPES experiment in fermiology of quasi-2D metals*”, *Low Temp. Phys.* **40**, 286 (2014).
- [41] C. C. Chang, “*Auger electron spectroscopy*”, *Surface Sci.* **25**, 53 (1971)
- [42] R. F. Egerton, “*Electron energy-loss spectroscopy in the TEM*”, *Rep. Prog. Phys.* **72**, 016502 (2009).
- [43] K. Hamalainen & S. Manninen, “*Resonant and non-resonant inelastic x-ray scattering*”, *J. Phys.: Condens. Matter* **13**, 7539 (2001).
- [44] M. O. Scully and M. S. Zubairy, *Quantum Optics* (Cambridge University Press, Cambridge, England, 1997).
- [45] Y. Yamamoto and A. Imamoglu, *Mesoscopic Quantum Optics* (John Wiley & Sons, New York, 1999).
- [46] Y. R. Shen, *The Principles of Nonlinear Optics* (John Wiley & Sons, New Jersey, 2003).
- [47] F. Vagizov, V. Antonov, Y.V. Radeonychev, R.N. Shakhmuratov, and O. Kocharovskaya, “*Coherent control of the waveforms of recoilless γ -ray photons*”, *Nature* **508**, 80 (2014).
- [48] R. Röhlsberger, K. Schlage, B. Sahoo, S. Couet, and R. Rüffer, “*Collective Lamb shift in single-photon superradiance*”, *Science* **328**, 1248 (2010).
- [49] R. Röhlsberger, H.-C. Wille, K. Schlage, and B. Sahoo, “*Electromagnetically induced transparency with resonant nuclei in a cavity*”, *Nature* **482**, 199 (2012).
- [50] C. K. Hong, Z. Y. Ou, and L. Mandel, “*Measurement of Subpicosecond Time Intervals between Two Photons by Interference*”, *Phys. Rev. Lett.* **59**, 2044 (1987).
- [51] J. S. Bell, “*On the Einstein Podolsky Rosen paradox*”, *Physics* **1**, 195 (1964).
- [52] D. Atwood, *Soft x-rays and extreme ultraviolet radiation: principles and applications* (Cambridge University Press, Cambridge, 1999)
- [53] M. Fuchs *et al.*, “*Anomalous nonlinear X-ray Compton scattering*”, *Nat. Phys.* **11**, 964 (2015).

- [54] S. E. Harris and S. Shwartz, “Parametric down conversion at x-ray wavelengths”, 21th INTERNATIONAL LASER PHYSICS WORKSHOP, Calgary, Canada (2012).
- [55] T. B. Pittman, Y. H. Shih, D. V. Strekalov, and A. V. Sergienko, “*Optical imaging by means of two-photon quantum entanglement*”, Phys. Rev. A **52**, R3429 (1995).
- [56] M. Yabashi, T. Mochizuki, H. Yamazaki, S. Goto, H. Ohashi, K. Takeshita, T. Ohata, T. Matsushita, K. Tamasaku, Y. Tanaka, and T. Ishikawa, “*Design of a beamline for the SPring-8 long undulator source I*” Nucl. Instrum. Methods Phys. Res., Sect. A **467**, 678 (2001).
- [57] J. Stempfer, S. Francoual, D. Reuther, D. K. Shukla, A. Skaugen, H. Schulte-Schrepping, T. Kracht, and H. Franz, “*Resonant scattering and diffraction beamline P09 at PETRA III*”, J. Synchrotron Rad. **20**, 541 (2013).
- [58] P. Grangier, G. Roger and A. Aspect, “*Experimental Evidence for a Photon Anticorrelation Effect on a Beam Splitter: A New Light on Single-Photon Interferences*”, Europhys. Lett. **1**, 173 (1986).
- [59] H. R. Phillip and E. A. Taft, “*Kramers-Kronig Analysis of Reflectance Data for Diamond*”, Phys. Rev. **136**, A1445 (1964).
- [60] B. L. Henke, E. M. Gullikson, and J. C. Davis, “*X-Ray Interactions: Photoabsorption, Scattering, Transmission, and Reflection at $E = 50\text{-}30,000$ eV, $Z = 1\text{-}92$* ”, At. Data Nucl. Data Tables **54**, 181 (1993).
- [61] S. Waidmann, M. Knupfer, B. Arnold, and J. Fink, “*Local-field effects and anisotropic plasmon dispersion in diamond*”, Phys. Rev. B **61**, 10149 (2000).
- [62] W. C. Walker and J. Osantowski, “*Unltraviolet Optical Properties of Diamond*”, Phys. Rev. **134**, A153 (1964).
- [63] R. Keown, “*Energy Bands in Diamond*”, Phys. Rev. **150**, 568 (1966).
- [64] M. Lucchini, S. A. Sato, A. Ludwig, J. Herrmann, M. Volkov, L. Kasmi, Y. Shinohara, K. Yabana, L. Gallmann, and U. Keller, “*Attosecond dynamical Franz-Keldysh effect in polycrystalline diamond*”, Science **353**, 916 (2016).
- [65] J.-P. Rueff, J. M. Ablett, D. Céolin, D. Prieur, T. Moreno, V. Balédent, B. Lassalle-Kaiser, J. E. Rault, M. Simon, and A. Shukla, “*The GALAXIES beamline at*

the SOLEIL synchrotron: inelastic X-ray scattering and photoelectron spectroscopy in the hard X-ray range”, J. Synchrotron Rad. **22**, 175 (2015).

[66] C. Kittel, *Introduction to Solid State Physics, 8th edition*, (John Wiley & Sons, New Jersey, 2005)

[67] D. Shoenberg, “*The Fermi Surfaces of Copper, Silver and Gold I. The de Haas-van Alphen Effect*”, Philos. Trans. R. Soc. Lond. A **255**, 85 (1962).

[68] J. Lindhard, “*On the properties of a gas of charged particles*”, Dan. Vidensk. Selsk. Mat.-Fys. Medd. **28**, 8 (1954).

[69] B. Mihaila, “*Lindhard functions of a d-dimensional Fermi gas*”, arXiv:1111.5337 [cond-mat.quant-gas] (2011).

[70] W. A. Caliebe, et al. “*Dynamic Structure Factor of Diamond and LiF Measured Using Inelastic X-Ray Scattering*”, Phys. Rev. Lett. **84**, 17, 3907 (2000).

[71] See <http://www.chembio.uoguelph.ca/educmat/atomdata/bindener/elecbind.htm> for tabulated values of electron binding energies; accessed 1 December 2018.

[72] V. Mauchamp, P. Moreau, G. Ouvard, and F. Boucher, “*Local field effects at Li K edges in electron energy-loss spectra of Li, Li₂O and LiF*”, Phys. Rev. B **77**, 045117 (2008).

[73] See http://henke.lbl.gov/optical_constants/asf.html accessed 1 December 2018.

[74] P. Abbamonte *et. al.*, “*Dynamical reconstruction of the exciton in LiF with inelastic x-ray scattering*”, Proc. Natl. Acad. Sci. U.S.A. **105**, 12159 (2008).

[75] Alex Zunger and A. J. Freeman, “*Ground- and excited-state properties of LiF in the local-density formalism*”, Phys. Rev. B **16**, 2901 (1977).

Appendix A

Solution of the coupled wave equations in the Heisenberg-Langevin picture

Consider the two wave equations under SVEA and undepleted pump approximation [16]:

$$\frac{\partial a_s}{\partial z} + \frac{\alpha_s}{\cos \theta_s} a_s = \kappa' a_i^+ \exp(i\Delta k_z z) + \sqrt{\frac{2\alpha_s}{\cos \theta_s}} f_s, \quad (\text{A1 a})$$

$$\frac{\partial a_i^+}{\partial z} + \frac{\alpha_i}{\cos \theta_i} a_i^+ = \kappa'^* a_s \exp(-i\Delta k_z z) + \sqrt{\frac{2\alpha_i}{\cos \theta_i}} f_i^+, \quad (\text{A1 b})$$

where a_s, a_i are the signal and the idler annihilation operators with the commutation relation

$$\begin{aligned} [a_j(z_1, \mathbf{q}_1, \omega_1), a_k^+(z_2, \mathbf{q}_2, \omega_2)] &= \\ &= \frac{1}{(2\pi)^3} \delta_{j,k} \delta(z_1 - z_2) \delta(\mathbf{q}_1 - \mathbf{q}_2) \delta(\omega_1 - \omega_2), \end{aligned} \quad (\text{A2})$$

the angles θ_s, θ_i are the signal and the idler angles taken from the solution of the phase matching equation (1.1), α_s, α_i are the absorption coefficients at the signal and idler

frequency respectively and $\kappa' = \frac{i\kappa}{\sqrt{\cos \theta_s \cos \theta_i}}$, where κ is the nonlinear coupling

coefficient. $\Delta k_z = k_p \cos \theta_p - k_s \cos \theta_s - k_i \cos \theta_i$ is the phase mismatch. We assume

that in the directions x, y phase matching conditions are preserved, k_j is a wave vector of the corresponding photon. The terms f_s, f_i are the Langevin noise operators that satisfy commutation relation

$$\begin{aligned} [f_j(z, \mathbf{q}, \omega), f_k^+(z', \mathbf{q}', \omega')] &= \\ &= \frac{1}{(2\pi)^3} \delta_{j,k} \delta(z-z') \delta(\mathbf{q}-\mathbf{q}') \delta(\omega-\omega'), \end{aligned} \quad (\text{A3})$$

where $\mathbf{q}_j = (k_{jx}, k_{jy})$ is the transverse wave vector, k_{jx} and k_{jy} are the wave-vector components parallel to the surfaces of the crystal, z is the direction normal to the surface of the crystal.

Introduce a matrix M :

$$M = \begin{bmatrix} \alpha_s + \frac{i\Delta k}{2} & -i\kappa \\ i\kappa & \alpha_i - \frac{i\Delta k}{2} \end{bmatrix}, \quad (\text{A4})$$

and find the solution of the system A1 using a matrix exponent $e^{-ML} = \begin{bmatrix} A & B \\ C & D \end{bmatrix}$ in the form:

$$\begin{pmatrix} a_s(L) \\ a_i^+(L) \end{pmatrix} = e^{-ML} \begin{pmatrix} a_s(0) \\ a_i^+(0) \end{pmatrix} + \int_0^L e^{M(z-L)} \begin{pmatrix} f_s(z) \\ f_i^+(z) \end{pmatrix} dz, \quad (\text{A5})$$

The solutions will be:

$$a_s(L) = Aa_s(0) + Ba_i^+(0) + \int_0^L E(z)f_s(z)dz + \int_0^L F(z)f_i^+(z)dz, \quad (\text{A6 a})$$

$$a_i^+(L) = Ca_s(0) + Da_i^+(0) + \int_0^L G(z)f_s(z)dz + \int_0^L H(z)f_i^+(z)dz, \quad (\text{A6 b})$$

where

$$E(z) = \begin{pmatrix} 1 & 0 \\ 0 & 0 \end{pmatrix} e^{M(z-L)} \sqrt{2\alpha_s} \begin{pmatrix} 1 \\ 0 \end{pmatrix}, \quad (\text{A7 a})$$

$$F(z) = \begin{pmatrix} 1 & 0 \\ 0 & 1 \end{pmatrix} e^{M(z-L)} \sqrt{2\alpha_i} \begin{pmatrix} 0 \\ 1 \end{pmatrix}, \quad (\text{A7 b})$$

$$G(z) = \begin{pmatrix} 0 & 1 \\ 0 & 1 \end{pmatrix} e^{M(z-L)} \sqrt{2\alpha_s} \begin{pmatrix} 1 \\ 0 \end{pmatrix}, \quad (\text{A7 c})$$

$$H(z) = \begin{pmatrix} 0 & 1 \\ 0 & 1 \end{pmatrix} e^{M(z-L)} \sqrt{2\alpha_s} \begin{pmatrix} 0 \\ 1 \end{pmatrix}, \quad (\text{A7 d})$$

The signal detector count rate is defined as $R_s = \langle a_s^+(t) a_s(t) \rangle$, which gives us the following expression:

$$\begin{aligned} R_s &= \langle a_s^+(t) a_s(t) \rangle = \\ &= \frac{1}{2\pi} \int_{\omega} |B(\omega)| d\omega + \frac{1}{2\pi} \int_{\omega} \int_0^L |F(z, \omega)|^2 d\omega dz. \end{aligned} \quad (\text{A8})$$

The coincidence count rate is defined as

$$R_{\text{coin}} = \text{Area} \iint G^{(2)}(\mathbf{u}, \tau) d\mathbf{u} d\tau, \quad (\text{A9})$$

where the integration is performed over the distance between the detectors $\mathbf{u} = \mathbf{r}_2 - \mathbf{r}_1$ and the time window $\tau = t_1 - t_2$. *Area* represents the factor of the illuminated area. One can obtain using the definition of the correlation function

$$G^{(2)}(\mathbf{u}, \tau) = \langle a_i^+(\mathbf{r}_2, t_2) a_s^+(\mathbf{r}_1, t_1) a_s(\mathbf{r}_1, t_1) a_i(\mathbf{r}_2, t_2) \rangle, \quad (\text{A10})$$

the following expression for the coincidence count rate

$$R_{\text{coin}} = \frac{\text{Area}}{2\pi} \left| \int_{\omega} A(\omega) C^*(\omega) d\omega + \left(\int_0^L E(\omega) G^*(\omega) dz \right) d\omega \right|^2, \quad (\text{A11})$$

Appendix B

Derivation of the nonlinear current density

Assumptions of the model:

1. We use the classical model for optical responses including the Lorentz force, the continuity equation, and Gauss's law in the form $\nabla \cdot \vec{E} = \frac{\rho_j^{(1)}}{\epsilon_0}$ [46], where E is the electric field strength and $\rho_j^{(1)}$ is the perturbed charge density at the j -th frequency.
2. The pump and the signal photon energies are much larger than the binding energy (i.e. atomic resonances).
3. We assume that the fields can be written as a sum of monochromatic plane waves in the form:

$$\vec{E}_j = \frac{1}{2} (E_j \exp(i(\vec{k}_j \vec{r} - \omega_j t)) + c.c.).$$

Derivation of the nonlinear current density:

The system of equations will then be [46]:

$$\frac{\partial \vec{v}}{\partial t} + (\vec{v} \cdot \nabla) \vec{v} + \omega_0^2 \vec{r} = -\frac{e}{m} (\vec{E} + \vec{v} \times \vec{B}), \quad (\text{B1})$$

$$\frac{\partial \rho}{\partial t} + \nabla \cdot (\rho \vec{v}) = 0, \quad (\text{B2})$$

where m_e is the effective electron mass, e is the electron electric charge, B is the magnetic field, E is the electric field strength of the corresponding wave, and ω_0 denotes the resonance frequency. We solve the equations by assuming that driving terms of the nonlinear interactions are much weaker than the driving terms of the linear interactions. We therefore expand the electric field, the electron velocity, and the electron density to the second order and separate terms with different harmonics according to the perturbation theory [46].

We get the following equation for the first order of each one of the fields:

$$\frac{\partial^2 \vec{r}}{\partial t^2} + \omega_0^2 \vec{r} = -\frac{e}{m} \vec{E}, \quad (\text{B3})$$

We use a Fourier transform of Eq. (A3) for the idler and the signal waves and obtain:

$$-\omega_p^2 \vec{r}_p + \omega_0^2 \vec{r}_p = -\frac{e}{m} \vec{E}_p, \quad (\text{B4})$$

$$-\omega_i^2 \vec{r}_i + \omega_0^2 \vec{r}_i = -\frac{e}{m} \vec{E}_i, \quad (\text{B5})$$

We solve this system of equations to obtain first order velocities ($\vec{v} = \dot{\vec{r}} = -i\omega\vec{r}$):

$$\vec{r}_{i,p}^{(1)} = -\frac{e}{m} \frac{\vec{E}_{i,p}}{\omega_0^2 - \omega_{i,p}^2}, \quad (\text{B6})$$

Recalling our assumption that the photon energy of the pump is much larger than the binding energy of the electrons we get the first order velocity:

$$\vec{v}_i^{(1)} = \frac{ie\omega_i \vec{E}_i}{m(\omega_0^2 - \omega_i^2)}, \quad (\text{B7})$$

$$\vec{v}_p^{(1)} = -\frac{ie\vec{E}_p}{m\omega_p}, \quad (\text{B8})$$

For the second order velocity, we obtain the following equation by looking for a solution for the velocity at the frequency $\omega_s = \omega_p - \omega_i$:

$$\frac{\partial^2 \vec{r}_s}{\partial t^2} + (\vec{v}^{(1)} \cdot \nabla) \vec{v}^{(1)} = -\frac{e}{m} (\vec{v}^{(1)} \times \vec{B}), \quad (\text{B9})$$

Next, we shift the convective derivative to the right hand side (R.H.S.) and write all the products explicitly:

$$\frac{\partial^2 \vec{r}_s}{\partial t^2} = -(\vec{v}_p^{(1)} \cdot \nabla) \vec{v}_i^{(1)*} - (\vec{v}_i^{(1)*} \cdot \nabla) \vec{v}_p^{(1)} - \frac{e}{m} (\vec{v}_i^{(1)*} \times \vec{B}_p) - \frac{e}{m} (\vec{v}_p^{(1)} \times \vec{B}_i^*), \quad (\text{B10})$$

From the Maxwell equations one can obtain $\vec{B} = -\frac{i}{\omega} \nabla \times \vec{E}$, and after substituting the first order velocities we get:

$$\begin{aligned} & \frac{e^2 \omega_i}{m^2 \omega_p (\omega_0^2 - \omega_i^2)} \left((\vec{E}_p \cdot \nabla) \vec{E}_i^* + (\vec{E}_i^* \cdot \nabla) \vec{E}_p \right) + \\ & + \frac{e^2 \omega_i}{m^2 \omega_p (\omega_0^2 - \omega_i^2)} \left(\vec{E}_i^* \times (\nabla \times \vec{E}_p) \right) - \frac{e^2}{m^2 \omega_p \omega_i} \left(\vec{E}_p \times (\nabla \times \vec{E}_i^*) \right), \quad (\text{B11}) \end{aligned}$$

Now we use the vector identity:

$$(\vec{A} \cdot \nabla) \vec{B} + (\vec{B} \cdot \nabla) \vec{A} = \nabla (\vec{A} \cdot \vec{B}) - \vec{A} \times (\nabla \times \vec{B}) - \vec{B} \times (\nabla \times \vec{A})$$

to eliminate one of the vector products in (B11) (remember that Eq. (B11) is the R.H.S. of Eq. (B10)). We then have:

$$\begin{aligned} & \frac{e^2 \omega_i}{m^2 \omega_p (\omega_0^2 - \omega_i^2)} \nabla (\vec{E}_p \cdot \vec{E}_i^*) - \\ & - \frac{e^2}{m^2 \omega_p} \left(\frac{\omega_i}{\omega_0^2 - \omega_i^2} + \frac{1}{\omega_i} \right) \vec{E}_p \times \nabla \times \vec{E}_i^*, \quad (\text{B12}) \end{aligned}$$

We repeat the steps used to obtain Eqs. (B3-B5) to write the second order velocity:

$$\vec{v}_s^{(2)} = \frac{ie^2}{m^2 \omega_s \omega_p (\omega_0^2 - \omega_i^2)} \left(\omega_i \nabla (\vec{E}_p \cdot \vec{E}_i^*) - \frac{\omega_0^2}{\omega_i} (\vec{E}_p \times \nabla \times \vec{E}_i^*) \right). \quad (\text{B13})$$

Now we obtain the expressions for the perturbed charge density:

$$\frac{\partial \rho}{\partial t} = -\nabla \cdot (\rho_0 \vec{v}), \quad (\text{B14})$$

$$\nabla \cdot (\rho_0 \vec{v}) = \vec{v} \cdot \nabla \rho_0 + \rho_0 \nabla \cdot \vec{v} . \quad (\text{B15})$$

We assume the unperturbed charge density to be $\rho_0(\vec{r}) = \sum_G \rho_G \exp(i\vec{G} \cdot \vec{r})$,

where G is a reciprocal lattice vector and ρ_G is the G -th Fourier coefficient of the

unperturbed charge density $\rho_G = \frac{1}{V} \int_V \rho_0(\vec{r}) \exp(-i\vec{G} \cdot \vec{r}) dv$. The integration is

performed over the unit cell volume V . **We assume that only one Fourier component corresponds to the process since we use only one reciprocal lattice vector for the phase-matching condition.**

$$-i\omega\rho^{(1)} = -(\vec{v} \cdot \nabla \rho_0 + \rho_0 \nabla \cdot \vec{v}) . \quad (\text{B16})$$

Now we substitute the first order velocity and obtain the charge density at the pump frequency:

$$i\omega_p \rho_p^{(1)} = -\frac{ie}{m\omega_p} (\vec{E}_p \cdot \nabla \rho_0 + \rho_0 \nabla \cdot \vec{E}_p)$$

$$\rho_p^{(1)} = \frac{e}{m\omega_p^2} (\vec{E}_p \cdot \nabla \rho_0 + \rho_0 \nabla \cdot \vec{E}_p) . \quad (\text{B17})$$

Now we use Gauss law [46] $\nabla \cdot \vec{E}_p = \frac{\rho_p^{(1)}}{\epsilon_0}$, substituting this into Eq. (B17) one can

get:

$$\rho_p^{(1)} = -\frac{e\vec{E}_p \cdot \nabla \rho_0}{m\omega_p \left(1 - \frac{\omega_{plasma}^2}{\omega_p^2}\right)} , \quad (\text{B18})$$

where $\omega_{plasma} = \sqrt{\frac{e\rho_0}{m\epsilon_0}}$. In the case of the pump frequency we can neglect the term

that includes the plasma resonant frequency, since $\frac{\omega_{plasma}^2}{\omega_p^2} \ll 1$.

We rewrite the gradient using the Fourier expansion of the unperturbed charge density

$\rho_0 = \rho_G \exp(i\vec{G} \cdot \vec{r})$ and obtain the final expression for the first order charge density:

$$\rho_p^{(1)} = -\frac{ie\rho_0}{m\omega_p^2} \vec{G} \cdot \vec{E}_p. \quad (\text{B19})$$

For the idler frequency we write:

$$\rho_i^{(1)} = -\frac{e}{m(\omega_o^2 - \omega_i^2)} (E_i \cdot \nabla \rho_0 + \rho_0 \nabla \cdot E_i), \quad (\text{B20})$$

$$\rho_i^{(1)} = \frac{ie\rho_0}{m(\omega_o^2 - \omega_i^2) \left(1 + \frac{\omega_{plasma}^2}{(\omega_o^2 - \omega_i^2)}\right)} \vec{G} \cdot \vec{E}_i. \quad (\text{B21})$$

The next step is to substitute each obtained expression (for the first and the second order velocities and perturbed charge densities) into the nonlinear current density expression:

$$\vec{J}_s^{NL} = \rho_0 \vec{v}_s^{(2)} + \rho_p^{(1)} \vec{v}_i^{(1)*} + \rho_i^{(1)*} \vec{v}_p^{(1)}, \quad (\text{B22})$$

$$\begin{aligned} \vec{J}_s^{NL} = & \frac{i\rho_0 e^2}{m^2 \omega_s \omega_p (\omega_o^2 - \omega_i^2)} \left(\omega_i \nabla (\vec{E}_p \cdot \vec{E}_i^*) - \frac{\omega_o^2}{\omega_i} (\vec{E}_p \times \nabla \times \vec{E}_i^*) \right) - \\ & - \frac{e^2 \rho_0 \omega_i \vec{G} \cdot \vec{E}_p}{m^2 \omega_p^2 (\omega_o^2 - \omega_i^2)} \vec{E}_i^* - \frac{e^2 \rho_0 \vec{G} \cdot \vec{E}_i}{m^2 \omega_p (\omega_o^2 - \omega_i^2) \left(1 + \frac{\omega_{plasma}^2}{(\omega_o^2 - \omega_i^2)}\right)} \vec{E}_p. \end{aligned} \quad (\text{B23})$$

The triple vector product in the left parenthesis can be rewritten by using our plane wave assumptions as:

$$\vec{E}_p \times \nabla \times \vec{E}_i^* = \vec{E}_p \times (k_i E_i \hat{y}), \quad (\text{B24})$$

where \hat{y} is a unity vector in a direction out of the scattering plane (if the scattering is on a sheet of paper then this vector would be toward us). Therefore if the pump beam is polarized (i.e. collinear with the y vector) out of the scattering plane this product would be zero. Writing the expression for the nonlinear current in this case we get:

$$\vec{J}_s^{NL} = \frac{\rho_0 e^2}{m^2 \omega_p (\omega_0^2 - \omega_i^2)} \left[\frac{\omega_i}{\omega_s} i \nabla (\vec{E}_p \cdot \vec{E}_i^*) - \frac{\omega_i \vec{G} \cdot \vec{E}_p}{\omega_p} \vec{E}_i^* - \frac{\vec{G} \cdot \vec{E}_i^*}{\left(1 + \frac{\omega_{plasma}^2}{(\omega_o^2 - \omega_i^2)}\right)} \vec{E}_p \right].$$

(B25)

We expand the left term in the brackets

$$i \nabla (\vec{E}_p \cdot \vec{E}_i^*) = -(\vec{k}_p - \vec{k}_i) (\vec{E}_p \cdot \vec{E}_i^*) . \quad (B26)$$

We neglect the left and the middle term in the brackets, since they are much smaller than the right term:

$$\vec{J}_s^{NL} = - \frac{\rho_0 e^2}{m^2 \omega_p (\omega_0^2 - \omega_i^2)} \left(\frac{\vec{G} \cdot \vec{E}_i^*}{\left(1 + \frac{\omega_{plasma}^2}{(\omega_o^2 - \omega_i^2)}\right)} \vec{E}_p \right). \quad (B27)$$

Now we project the current density onto the field direction of the generated radiation (scalar product of the nonlinear current and a unit vector $\hat{e}_s \perp \vec{k}_s$). Also from the phase-matching conditions we have $\vec{k}_p - \vec{k}_i = \vec{k}_s - \vec{G}$, resulting in:

$$\vec{J}_s^{NL} \cdot \hat{e}_s = \frac{\rho_0 e^2}{m^2 \omega_p (\omega_0^2 - \omega_i^2)} \left(- \frac{(\vec{G} \cdot \vec{E}_i^*) (\vec{E}_p \cdot \hat{e}_s)}{\left(1 - \frac{\omega_{plasma}^2}{(\omega_o^2 - \omega_i^2)}\right)} \right). \quad (B28)$$

Next we get:

$$\vec{J}_s^{NL} \cdot \hat{e}_s = \frac{\rho_0 e^2 E_i^* E_p}{m^2 \omega_p (\omega_0^2 - \omega_i^2)} \left(- \frac{(\vec{G} \cdot \hat{e}_i) (\hat{e}_p \cdot \hat{e}_s)}{\left(1 + \frac{\omega_{plasma}^2}{(\omega_o^2 - \omega_i^2)}\right)} \right). \quad (B29)$$

Recalling that only one reciprocal lattice vector is used for the phase-matching condition, we write only the corresponding Fourier component of the nonlinear current density that contributes to the nonlinear process:

$$\vec{J}_G^{NL}(\omega_s) \cdot \hat{e}_s = \frac{\varepsilon_0 e \chi_G^{(1)}(\omega_i) E_i^* E_p}{m^2 \omega_p} \left(- \frac{(\vec{G} \cdot \hat{e}_i)(\hat{e}_p \cdot \hat{e}_s)}{\left(1 + \frac{\omega_{plasma}^2}{(\omega_o^2 - \omega_i^2)} \right)} \right), \quad (\text{B30})$$

where $\chi_G^{(1)}(\omega_i) = \frac{e \rho_G}{\varepsilon_0 (\omega_o^2 - \omega_i^2)}$ is the G-th Fourier component of the linear electric susceptibility.

Appendix C

Papers in peer review journals

In this Appendix I provide a list of the published papers:

1. D. Borodin, A. Schori, F. Zontone, and S. Shwartz, "*X-ray photon pairs with highly suppressed background*", Phys. Rev. A **94**, 013843 (2016).
2. D. Borodin, S. Levy, and S. Shwartz, "*High energy-resolution measurements of x-ray into ultraviolet parametric down-conversion with an x-ray tube source*", Appl. Phys. Lett. **110**, 131101 (2017).
3. D. Borodin, A. Schori, J.-P. Rueff, J.M. Ablett, and S. Shwartz, "*Evidence for Collective Nonlinear Interactions in X Ray into Ultraviolet Parametric Down-Conversion*", Phys. Rev. Lett. **122**, 023902 (2019).

תקציר

במסגרת מחקר הדוקטורט שלי, חקרתי אספקטים שונים לשימושים באפקט "המרת תדר פרמטרית" בתחום קרינת רנטגן. בעבודת התזה הזו מפורטים שני חלקי המחקר, השונים בתדרי ההמרה: המרת תדר פרמטרית של קרינת רנטגן לתחום קרינת רנטגן, והמרת תדר פרמטרית לתחום קרינה אולטרה סגולה.

ידיעותינו הן בתאוריה והן בניסויים באופטיקה לא לינארית בתחום קרינת הרנטגן, מעט מוגבלת בהשוואה לתחום התדרים הנראה בספקטרום האלקטרומגנטי. בתחום הנראה ההשפעה של אופטיקה לא-לינארית היא עצומה. הסיבה להבדלים בידע על התהליך הלא לינארי בתחום תדרי הרנטגן בהשוואה לתחום הנראה היא הגודל של הסדר השני של מקדם הסוספטביליות הלא לינארי. מקדם הסוספטביליות תלוי בתדר, וערכו בתחום קרינת הרנטגן הוא בערך 7-10 סדרי גודל קטן יותר ממערכו בתחום הנראה.

בימנו יכולות מקורות קרינת רנטגן חזקים, כמו מתקני סינכורון דור שלישי, ולייזר אלקטרוניים חופשיים בתחום הרנטגן, מאפשרים להרחיב את הלמידה הניסיונית באופטיקה לא לינארית בתחום הרנטגן. אחד מהתהליכים המעניינים והבסיסיים מסדר שני הוא תהליך המרת תדר פרמטרית בתחום הרנטגן.

המרת תדר פרמטרית הוא תהליך מסדר שני בו הפוטונים השואבים עושים אינטרקציה עם הפלקטואציות של הוואקום דרך החומר הלא לינארי. כתוצאה מכך נפלטים שני פוטונים הנקראים "signal" ו "idler". המרת תדר פרמטרית בתחום הנראה היא תופעה מוכרת ושימשה רבות בעבר כמקור קרינה קוונטי בעוד שהתופעה בתחום תדרי הרנטגן נשאר תחום מחקר פתוח. תהליך המרת התדר בתחום הרנטגן הוא תהליך לא לינארי מעניין בפני עצמו, בנוסף יש לו ישום חשוב במדידת צפיפות אלקטרוני הערכיות.

החלק הראשון בעבודתי מוקדש למחקר תהליך המרת תדר פרמטרית של קרינת רנטגן לתחום קרינת רנטגן. כמו בתחום הנראה, תהליך זה יכול לשמש כמקור קרינה קוונטי. מקורות קרינה קוונטים זוכים לעניין רב, כמו גם בתחום הרנטגן. האתגר בתהליך הוא לקבל קצב סביר ולא זניח, של זוגות פוטונים. יש לקחת בחשבון שמעלים את עוצמת המקור כל תהליכי הפיזור הלינארי (פיזור אלסטי, קומפטון ופלורסנציה) גדלים ויכולים לגרום לרוויה בגלאים. אני מתאר גישה ליצור זוגות

פוטונים הנוצרים בקירוב באותו כיוון, כשרעש הרקע מינימלי. מערכת הניסוי שבניתי ואתאר בהמשך, משמשת לשאר הניסויים בתחום יצירת זוגות הפוטונים.

החלק השני בעבודתי מתאר את המחקר של תהליך המרת תדר פרמטרית של קרינת רנטגן לתחום קרינת אולטרה סגול. ידוע כי תהליך זה יכול לשמש למדידת אלקטרונים ומכך ללמוד על תכונות חומרים. כמו כן, בהסתמך על העקרונות של תהליך זה ניתן לפתח שיטה חדשה בספקטרוסקופיה. אפרט בעבודה זו את השלבים החיוניים להבנה מעמיקה של תהליך המרת תדר פרמטרית מקרינת רנטגן לקרינה בתחום האולטרה סגול.

תחילה אציג מודל תאורטי תגובה לא ליניארית של חומרים לתופעות קולקטיביות: אינטרקציה בין פלזמונים באזור הפנימי עם הרזוננס של האלקטרונים. המודל חוזה תכונה ספקטרלית המתאימה לאינטרקציה הלא ליניארית ולא לרזוננסים אטומיים. הדגמתי בפעם הראשונה תהליך של המרת תדר פרמטרית בקרינת רנטגן לקרינה על סגולה בגביש יהלום, זו הוכחה ברורה לאינטרקציה עם פלזמונים באיזור הפנימי.

לאחר מכן אציג תוצאות מדידה של המרת תדר פרמטרית של קרינת רנטגן לקרינה בתחום אולטרה סגול במתכות. אציג תוצאות מגביש אלומינים המוכיחות תגובה של אנרגית פרמי – אפקט אלקטרוני קולקטיבי.

לבסוף, אני מדווח על מדידות המרת תדר פרמטרית של קרינת רנטגן לקרינה בתחום אולטרה סגול ביהלום ובגביש ליתיום פלוריד במקור קרינת רנטגן מעבדתי, בניגוד למחקרים אחרים בהם מקור הקרינה היה בסינכטרון. חלק זה חשוב מאוד כיוון שמציג את היכולות של מדידות אלו במחקר נרחב בפיסיקה ובכימיה. אני מאמין שמחקר זה יצית את העניין בספקטרוסקופיה המבוססת על המרת תדר פרמטרית מקרינת רנטגן לתחום קרינת האולטרה סגול.

תוכן העניינים

i	תקציר אנגלי
1	1. הקדמה ורקע
1	1.1 סקירת ספרות
3	1.1.1 המרת קרינת רנטגן להמרת תדר פרמטרית
5	1.1.2 ספקטרוסקופיה לא לינארית בתחום הרנטגן
10	1.2 משוואות הגלים המצומדות
12	1.3 צפיפות זרם לא לינארית
15	2. המרת תדר פרמטרית כמקור לזוגות פוטונים
15	2.1 זוגות פוטונים בתחום הרנטגן בהנחתת רעש רקע
15	2.1.1 הקדמה
16	2.1.2 בסיס תאורטי
19	2.1.3 הניסוי
21	2.1.4 תוצאות ודיון
25	2.2 שיתוף פעולה
29	3. ספקטרוסקופיה לא לינארית בתחום הרנטגן
	3.1 הוכחת אינטראקציות קולקטיביות של קרינת רנטגן לתחום אולטרה סגול
29	3.1.1 הקדמה
30	3.1.2 המודל
33	3.1.3 מהלך הניסוי

35	3.1.4	מדידות ספקטרליות ודיון
37	3.2	תגובה אופטית לא לינארית במתכות
37	3.2.1	הקדמה
38	3.2.2	התבססות הניסוי
40	3.2.3	ספקטרום האלומיניום ודיון
	3.3	מדידות מרזולוציה אנרגטית גבוהה של המרת תדר פרמטרית מקרינת רנטגן לתחום אולטרה סגול עם מקור קרינה מעבדתי
42		
42	3.3.1	הקדמה
44	3.3.2	מערכת הניסוי והערכת רעש הרקע
47	3.3.3	מהלך הניסוי ותוצאות
51	3.3.4	ספקטרום גביש ליתיום פלוריד ודיון
53	4	מסקנות והצעות לעתיד
53	4.1	סיכום התרומה שלי למחקר
55	4.2	המשך המחקר בעתיד
57		ביבליוגרפיה
63		נספח A - חישוב משוואת צימוד גלים בתמונת היזנברג- לנג'וין
66		נספח B - חישוב נגזרת צפיפות מטען לא לינארי
73		נספח C - מאמרים שפרסמתי בעיתונים עם ביקורת עמיתים
		תקציר
		א

עבודה זו נעשתה בהנחייתו של

פרופ' שרון שוורץ

המחלקה לפיסיקה
אוניברסיטת בר-אילן

**יישומי המרת תדר פרמטרית בספקטרוסקופיה לא לינארית בקרני
רנטגן ואופטיקה קוונטית**

חיבור לשם קבלת התואר "דוקטור לפילוסופיה"

מאת:

דניס בורודין

המחלקה לפיסיקה

הוגש לסנט של אוניברסיטת בר-אילן

טבת, תשע"ח

רמת גן